

# Super-Eddington QSO RX J0439.6-5311. II. Multi-wavelength Constraints on the Global Structure of the Accretion Flow

Chichuan Jin<sup>1\*</sup>, Chris Done<sup>2</sup>, Martin Ward<sup>2</sup>, Emma Gardner<sup>1</sup>

<sup>1</sup>Max-Planck-Institut für Extraterrestrische Physik, Giessenbachstrasse, D-85748 Garching, Germany

<sup>2</sup>Centre for Extragalactic Astronomy, Department of Physics, University of Durham, South Road, Durham DH1 3LE, UK

prepared for MNRAS

## ABSTRACT

We present a detailed multi-wavelength study of an unobscured, highly super-Eddington Type-1 QSO RX J0439.6-5311. We combine the latest *XMM-Newton* observation with all archival data from infrared to hard X-rays. The optical spectrum is very similar to that of 1H 0707-495 in having extremely weak [O III] and strong Fe II emission lines, although the black hole mass is probably slightly higher at  $5 - 10 \times 10^6 M_{\odot}$ . The broadband SED is uniquely well defined due to the extremely low Galactic and intrinsic absorption, so the bolometric luminosity is tightly constrained. The optical/UV accretion disc continuum is seen down to 900 Å, showing that there is a standard thin disc structure down to  $R \geq 190-380 R_g$  and determining the mass accretion rate through the outer disc. This predicts a much higher bolometric luminosity than observed, indicating that there must be strong wind and/or advective energy losses from the inner disc, as expected for a highly super-Eddington accretion flow. Significant outflows are detected in both the NLR and BLR emission lines, confirming the presence of a wind. We propose a global picture for the structure of a super-Eddington accretion flow where the inner disc puffs up, shielding much of the potential NLR material, and show how inclination angle with respect to this and the wind can explain very different X-ray properties of RX J0439.6-5311 and 1H 0707-495. Therefore, this source provides strong supporting evidence that ‘simple’ and ‘complex’ super-Eddington NLS1s can be unified within the same accretion flow scenario but with different inclination angles. We also propose that these extreme NLS1s could be the low-redshift analogs of weak emission-line quasars (WLQs).

**Key words:** accretion, accretion discs - galaxies: active - galaxies: nuclei.

## 1 INTRODUCTION

Active Galactic Nuclei (AGN) are powered by the accretion of material onto a super-massive black hole (SMBH). Hence their emission should be determined mainly by the fundamental parameters of mass and spin of the black hole together with mass accretion rate, while inclination angle can also affect the observed properties. The current zoo of AGN subtypes should then map to these parameters. Boroson (2002) show how the optical spectra of different types of unobscured AGN can be decomposed in terms of principle components (PC), and that the most important (PC1: weak [O III], strong Fe II and narrow H $\beta$ ; PC2: weak He II) corresponded to increasing luminosity relative to Eddington,

$L/L_{\text{Edd}}$  and total luminosity, respectively. This identifies the optical class of Narrow Line Seyfert 1 (NLS1) galaxies (Osterbrock & Pogge 1985) as powered by high  $L/L_{\text{Edd}}$  accretion onto a low mass ( $\lesssim 10^7 M_{\odot}$ ) black hole.

NLS1s also typically show strong soft X-ray emission (below 2 keV: Boller, Brandt & Fink 1996), and a steeper 2-10 keV X-ray spectrum than broad line Seyfert 1s (Brandt, Mathur & Elvis 1997). Extrapolating their 2-10 keV spectra down below 2 keV reveals a strong soft X-ray excess above the prediction of a single power law. This excess is interpreted as some combination of either relativistically smeared, ionised reflection from the inner disc (e.g. Miniutti & Fabian 2004; Ross & Fabian 2005; Fabian & Miniutti 2005; Crummy et al. 2006; Fabian et al. 2013), Comptonisation from an additional electron population at  $\sim 0.2$  keV (e.g. Laor et al. 1997; Magdziarz et al. 1998; Gierliński &

\* E-mail: chichuan@mpe.mpg.de

Done 2004; Done et al. 2012 hereafter D12), and intrinsic emission from the accretion disc itself (D12; Jin et al. 2013; Chiang et al. 2015).

The 2-10 keV X-rays are variable on short timescales, as expected for a low mass black hole (e.g. Ponti et al. 2012). However, some fraction of NLS1s show extreme variability amplitudes, with strong spectral variability seen in low flux states, where their 2-10 keV spectra are much flatter, with extremely strong features seen around the iron K shell energy at 6-8 keV (Gallo 2006). The spectra of these ‘complex’ NLS1s (as opposed to the ‘simple’ NLS1s described above: Gallo 2006) have been variously interpreted as being dominated by highly relativistic ionised reflection from the very inner disc (Fabian et al. 2013); and/or absorption and scattering by material in a wind (e.g. Turner et al. 2007; Miller et al. 2007; Sim et al. 2010; Tatum et al. 2012; Gardner & Done 2015; Hagino et al. 2016). The best known examples of this complex NLS1 class are 1H 0707-495 and IRAS13224-3809 (Leighly & Moore 2004; Ponti et al. 2010; Chiang et al. 2015; Parker et al. 2017), while well known ‘simple’ ones are PG 1244+026 RE J1034+324 (the QPO AGN: Gierliński et al. 2008; Jin et al. 2013), Ton S180 and Akn 564 (Gallo 2006).

Understanding the accretion flow in NLS1 requires breaking the spectral degeneracies which underlie these different physical models. One way to do this is to extend the bandpass to study the broader Spectral Energy Distribution (SED), to set the X-ray spectrum in a multi-wavelength context. Optical/UV data in particular can constrain the two key parameters of both mass and mass accretion rate. Done & Jin (2016) (hereafter: DJ16) compared two well studied NLS1s, PG 1244+026 as an archetypal ‘simple’ NLS1 and 1H 0707-495 as a archetypal ‘complex’ NLS1. Both sources have similarly low black hole masses (similarly narrow H $\beta$  line, similar optical continuum luminosity) and similar absolute mass accretion rates,  $\dot{M}$ , (determined from the optical continuum:  $F_{\text{opt}} \propto \cos i (M\dot{M})^{2/3}$ , Davis & Laor 2011). Both are then similarly at Eddington or above even for the highest possible mass, zero spin and low inclination angle (DJ16). Low mass, high spin and high inclination (as derived for 1H 0707-495 from reverberation mapping assuming an inner disc reflection dominated spectrum e.g. Fabian et al. 2009; Zoghbi et al. 2010; Kara et al. 2013) mean that the mass accretion rate is extremely super-Eddington, implying  $L \geq 150 L_{\text{Edd}}$  for 1H 0707-495 (DJ16).

A highly super-Eddington accretion flow is very likely to power a wind (Ohsuga & Mineshige 2011; Jiang, Davis & Stone 2014; Takeuchi, Ohsuga & Mineshige 2014). This energy loss can explain the apparent discrepancy between the observed X-ray spectrum and the much higher X-ray flux predicted by a standard accretion disc spectrum in both PG 1244+026 and 1H 0707-495 (DJ16), as well as in the intermediate-mass black hole RX J1140.1+0307 (Jin, Done & Ward 2016). In the presence of a clumpy disc wind, the difference between ‘simple’ and ‘complex’ NLS1s can be explained as due to different inclination angles (DJ16). Gardner & Done (2015) showed that absorption caused by gas clumps above the disc with different viewing angles can reproduce the observed time lag transition from the 200 s hard X-ray reverberation lag in PG 1244+026 to the 30 s lag in 1H 0707-495. Hagino et al. (2016) showed that absorption by wind clumps can also reproduce the X-ray spectra of

1H 0707-495 above 2 keV, including the broad iron K $\alpha$  feature, without requiring any extreme relativistic smearing or super-solar iron abundance (see also the recent detection of blueshifted absorption from a wind in the complex NLS1 IRAS13224+3809: Parker et al. 2017). These studies support the view that it is the inclination angle which is the key parameter separating the two X-ray classes of NLS1s.

However, there are some other differences between PG 1244+026 and 1H 0707-495 which cannot be explained as being solely due to different inclination angles. For example, forbidden lines such as the [O III] $\lambda$ 4959/5007 doublets are much weaker in 1H 0707-495 than in PG 1244+026. These make 1H 0707-495 appear more extreme on PC1 (Boroson 2002), implying higher  $L/L_{\text{Edd}}$  than in PG 1244+026. Given that they have the same optical flux, the  $\cos i$  dependence of the accretion disc emission means that this does imply a higher  $L/L_{\text{Edd}}$  for 1H 0707-495, even if it has the same mass and spin as PG 1244+026. For super-Eddington fluxes, the inner disc is expected to puff up, shielding more and more of the narrow line region (NLR) clouds for higher  $L/L_{\text{Edd}}$ , hence reducing the [O III] flux (e.g. Leighly 2004; Luo et al. 2015).

In any case, the inclination angle scenario predicts that there should be super-Eddington NLS1s with X-ray spectra similar to ‘simple’ NLS1s like PG 1244+026, but weak NLR lines similar to 1H 0707-495. Recently, Jin, Done & Ward (2017) (hereafter: Paper-I) presented a detailed X-ray analysis of such an AGN, namely RX J0439.6-5311, which has the smallest H $\beta$  full-width-at-half-maximum (FWHM) of  $700 \pm 140 \text{ km s}^{-1}$ , and the highest Eddington ratio of 12.9 among the 110 AGN in Grupe et al. (2004) (also see Grupe et al. 2011). Paper-I showed that the X-ray spectral-timing properties of this source are similar to PG 1244+026, but with even steeper 2-10 keV spectral index potentially indicating higher  $L/L_{\text{Edd}}$  (e.g. Shemmer et al. 2006). Here we collect archival data (Section 2) and show that it has an optical spectrum which is very similar to 1H 0707-495, with extremely weak [O III] and strong Fe II (Section 3). The full multi-wavelength spectral energy distribution (SED) is presented in Section 4, where the extremely low Galactic extinction of  $N_{\text{H}} = 7.45 \times 10^{19} \text{ cm}^{-2}$  (Kalberla et al. 2005) and low intrinsic extinction (Paper-I) mean that the spectrum is uniquely well defined. The high-quality *HST* spectra gives UV data up to  $\sim 10 \text{ eV}$  in the rest frame of RX J0439.6-5311, while the ROSAT data extends the X-ray spectrum from *XMM-Newton* down to 0.1 keV, so the bolometric luminosity is constrained to better than 20%. Section 5 shows constraints on short and long-term multi-wavelength variability of this SED. Section 6 shows physical models of the accretion flow for the estimated black hole mass and mass accretion rate. We clearly show that the mass accretion rate through the outer disc is super-Eddington, and that this does not convert to observed luminosity as expected for a geometrically thin disc. Instead, at least half of the expected luminosity is lost, probably powering a wind. We build a global picture of accretion flows in all super-Eddington NLS1s and compare these NLS1s with weak emission-line quasars at high redshifts. The final section summarises the main results of this paper. Throughout this paper we adopt a flat universe model for the luminosity distance with the Hubble constant  $H_0 = 72 \text{ km s}^{-1} \text{ Mpc}^{-1}$ ,  $\Omega_{\Lambda} = 0.73$  and  $\Omega_{\text{M}} = 0.27$ .

**Table 1.** Multi-wavelength data of RX J0439.6-5311 analysed in this work. ‘Exp’ is the exposure time. The *WISE* observation (denoted by †) was from 2010-01-28 to 2010-01-30, consisting of 37 separate exposures. The *WISE* observation on 2010-08-06 consisted of 2 separate exposures, but we cannot find the exposure time for *WISE* and *2MASS*.

| Instrument                  | Obs-Date    | Exp (ks) | Waveband            |
|-----------------------------|-------------|----------|---------------------|
| <i>XMM-Newton</i> EPIC/OM   | 2016-02-12  | 120      | X-ray/UV/Optical    |
| <i>ROSAT</i> PSPCB          | 1997-02-20  | 1.3      | Soft X-ray          |
| <i>ROSAT</i> PSPCB          | 1997-02-20  | 0.7      | Soft X-ray          |
| <i>ROSAT</i> PSPCB          | 1997-02-26  | 0.6      | Soft X-ray          |
| <i>Swift</i> XRT/UVOT       | 2006-01-06  | 5.4      | X-ray/UV/Optical    |
| <i>Swift</i> XRT/UVOT       | 2006-04-13  | 4.0      | X-ray/UV/Optical    |
| <i>Swift</i> XRT/UVOT       | 2006-04-15  | 4.3      | X-ray/UV/Optical    |
| <i>Swift</i> XRT/UVOT       | 2006-05-18  | 3.4      | X-ray/UV/Optical    |
| <i>Swift</i> XRT/UVOT       | 2012-05-09  | 1.0      | X-ray/UV/Optical    |
| <i>Swift</i> XRT/UVOT       | 2012-05-14  | 1.5      | X-ray/UV/Optical    |
| <i>Swift</i> XRT/UVOT       | 2014-04-05  | 1.0      | X-ray/UV/Optical    |
| <i>Swift</i> XRT/UVOT       | 2014-04-17  | 0.9      | X-ray/UV/Optical    |
| <i>HST</i> COS              | 2010-02-07  | 2.2      | UV (G130M)          |
| <i>HST</i> COS              | 2010-02-07  | 1.0      | UV (G130M)          |
| <i>HST</i> COS              | 2010-02-07  | 2.0      | UV (G130M)          |
| <i>HST</i> COS              | 2010-02-07  | 1.0      | UV (G130M)          |
| <i>HST</i> COS              | 2010-02-07  | 2.0      | UV (G130M)          |
| <i>HST</i> COS              | 2010-02-07  | 0.8      | UV (G160M)          |
| <i>HST</i> COS              | 2010-02-07  | 3.7      | UV (G160M)          |
| <i>HST</i> COS              | 2010-02-07  | 2.2      | UV (G160M)          |
| <i>HST</i> COS              | 2010-02-07  | 2.2      | UV (G160M)          |
| <i>HST</i> COS              | 2010-05-26  | 4.2      | UV (G285M)          |
| <i>ESO 1.52 m Telescope</i> | 1999-09-14  | 2.7      | Optical             |
| <i>WISE</i>                 | 2010-01-30† | –        | Infrared (Band 1-4) |
| <i>WISE</i>                 | 2010-08-06  | –        | Infrared (Band 1-4) |
| <i>2MASS</i>                | 1999-11-05  | –        | Infrared (J, H, K)  |

## 2 MULTI-WAVELENGTH OBSERVATIONS

### 2.1 Data Collection

The latest 133 ks *XMM-Newton* (Jansen et al. 2001) data of RX J0439.6-5311 was obtained on 2016-02-12 (PI: C. Jin). During the observation, all the three European Photon Imaging Cameras (EPIC) (pn, MOS1, MOS2) were operating in the *Imaging* mode. The Reflection Grating Spectrometer (RGS) cameras were in the *Spectroscopy* mode. The Optical Monitor (OM) was in the *Imaging+Fast* mode with about 10 ks exposure in each of the V, B, U, UVM2, UVW2 bands and about 70 ks continuous exposure in the UVW1 band.

We also searched various public archives for existing multi-wavelength observations of RX J0439.6-5311, and found a collection of datasets from infrared (IR) to hard X-rays (Table 1):

(1) In the X-ray band RX J0439.6-5311 was observed by *ROSAT* PSPCB in 1997 with three short exposures, which extend the X-ray spectral coverage down to  $\sim 0.1$  keV. RX J0439.6-5311 was also observed by *Swift* in 2006, 2012 and 2014 with totally nine observations, including five observations in 2006, two observations in 2012 and two observations in 2014. One observation in 2006 is excluded because its exposure time was very short (only 429 s). The remaining eight observations were conducted with the X-ray telescope (XRT) in the photon counting (PC) mode and simultane-

ous exposures in the UV/Optical Telescope (UVOT). The observation on 2014-4-17 has only U-band exposures, while all the other observations have exposures in all six UVOT bands (i.e. U, B, V, UVW1, UVM2, UVW2). Since all the *Swift* exposures are much shorter than the *XMM-Newton* observation which provides high signal-to-noise (S/N) spectra in the same X-ray band, we only use the *Swift* data to study long-term variability.

(2) In the optical band we use the highest quality optical spectrum of RX J0439.6-5311, which was obtained by the European Southern Observatory (ESO) 1.52 m telescope in 1999 (Grupe et al. 2004a).

(3) In the UV band, Hubble Space Telescope (*HST*) observed RX J0439.6-5311 in 2010 with the Cosmic Origins Spectrograph (COS) instrument (PI: J. Green) in order to obtain high S/N detections of the emission/absorption-line system in the near/far-UV band. There are also *WISE* and *2MASS* photometric points in the near infrared (IR) band. Note that these *WISE* observations were obtained only one week earlier than the *HST* observations on 2017-02-07, so they can be considered as nearly simultaneous observations in the IR and UV bands. Since RX J0439.6-5311 has very low extinction along the line of sight, these datasets provide direct multi-wavelength information for the super-Eddington accretion flow in RX J0439.6-5311, which we present in the following sections.

### 2.2 Data Reduction

For the *XMM-Newton* observation, we reduced the data using the SAS software (v15.0.0) and the latest calibration files. High background periods were subtracted and no photon pile-up was found (see Paper-I for a complete description). In this paper we only use the EPIC-pn data with good events (FLAG=0) and PATTERN  $\leq 4$ . The source spectrum and light curve were extracted from a circular region of 80 arcsec centred at RX J0439.6-5311, with the background measured from a nearby source-free region of the same size. OM light curves were created by the `omfchain` task, with the background measured from the image data and subtracted automatically. For every OM filter the mean source count rate was extracted from the OM source-list file and put into the template file ‘om\_filter\_default.pi’, which was then combined with the latest canned response file using the `grppha` task for later spectral analysis<sup>1</sup> (also see Jin et al. 2013, hereafter: J13).

We downloaded the *ROSAT* data from the High Energy Astrophysics Science Archive Research Center (HEASARC) data archive and followed the standard data reduction procedure<sup>2</sup> and used XSELECT (v2.4d) to extract source and background spectra. The `pcarf` task was run to generate auxiliary files and response matrices. Since the three *ROSAT* observations were all conducted within one week (see Table 1), we combined their spectra using the `addspec` task (FTOOL v6.19) to maximise the S/N.

*Swift* data were also downloaded from the HEASARC

<sup>1</sup> We notice that this OM data preparation procedure is now integrated into the SAS `om2pha` task, which produces the same spectral file.

<sup>2</sup> [http://heasarc.gsfc.nasa.gov/docs/rosat/ros\\_xselect\\_guide/](http://heasarc.gsfc.nasa.gov/docs/rosat/ros_xselect_guide/)

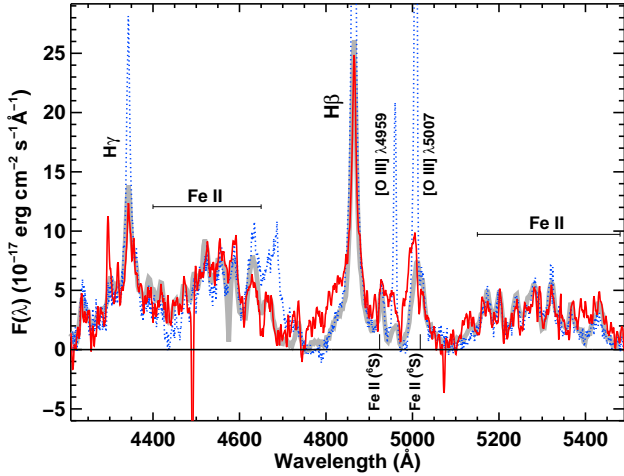


**Figure 1.** Comparison of optical emission lines between PG 1244+026 (dotted blue), 1H 0707-495 (thick gray) and RX J0439.6-5311 (solid red, smoothed by a factor of 5 to increase the visibility). Local underlying continua have been subtracted for every source. The line intensities of PG 1244+026 and 1H 0707-495 are rescaled to match the Fe II lines of RX J0439.6-5311 within 5100-5500Å. Both RX J0439.6-5311 and 1H 0707-495 show much weaker NLR lines than PG 1244+026.

data archive. Standard data reduction procedures were followed according to the official threads<sup>3</sup>, using the softwares provided in the HEASOFT (v6.19) package and latest calibration files in the calibration database (CALDB). For the XRT data, the `xrtpipeline` task (HEASOFT v6.19) was used to reprocess the data and produce the event file. Then the images, source and background spectra were extracted within the XSELECT environment, including a standard check for the photon pile up (not found). Auxiliary files were produced using the `xrtmkarf` task for spectral analysis. For the UVOT data, the `uvotimsum` and `uvot2pha` tasks were used to sum exposures and create spectral files for every filter.

The *HST* spectra of RX J0439.6-5311 have been well calibrated and analysed by Danforth et al. (2016) in order to probe the foreground intergalactic medium by using the well resolved absorption lines (also see Keeney et al. 2013). The calibrated and combined spectra were downloaded directly from the Mikulski Archive for Space Telescopes (MAST), where a sophisticated line detection procedure has also been performed (Danforth et al. 2016).

### 3 OPTICAL/UV SPECTRAL CONSTRAINTS

#### 3.1 The Redshift of RX J0439.6-5311

An optical spectrum can provide direct constraints on the black hole mass and mass accretion rate, and also provide information about different emission line regions (NLR and broad line region: BLR). The redshift of RX J0439.6-5311 given in the NASA/IPAC EXTRAGALACTIC DATABASE (NED) is 0.243 with no quoted error, which was originally

<sup>3</sup> <http://www.swift.ac.uk/analysis/>

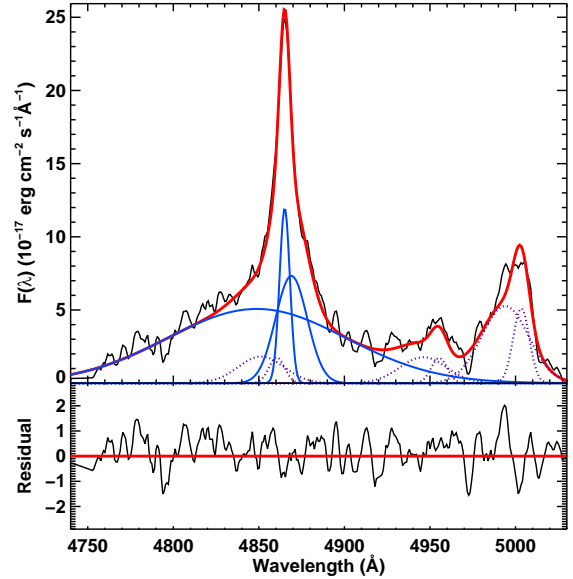


**Figure 2.** Multi-Gaussian fit to the H $\beta$  line and [O III] $\lambda$ 4959/ $\lambda$ 5007 doublets in RX J0439.6-5311. The spectrum is smoothed by a factor of 5 to increase the visibility. The Fe II lines have been subtracted. Dotted profiles show the Gaussian components for the NLR lines. Solid blue profiles show the Gaussian components for the BLR lines. See Section 3 for detailed fitting strategy. The lower panel shows the residuals (i.e. data - model).

reported by Thomas et al. (1998). Since RX J0439.6-5311 has very weak NLR lines and the original spectrum has low resolution (FWHM=30Å), this redshift may not be very accurate. In order to obtain a more accurate redshift estimate, we match the optical lines of RX J0439.6-5311 with those of PG 1244+026, whose redshift is precisely measured to be  $z = 0.0482 \pm 0.0008$  from its strong NLR lines. In this way, we find  $z = 0.242$  to be a more accurate redshift for RX J0439.6-5311, which results in a good matching of most optical lines with PG 1244+026, except the [O III] $\lambda$ 4959, 5007 doublets which are clearly weaker, broader and more blueshifted in RX J0439.6-5311 than in PG 1244+026 (Fig. 1). Next we add 1H 0707-495 for comparison ( $z = 0.0398$ , DJ16). It is clear that RX J0439.6-5311 is more similar to 1H 0707-495 in terms of the strength of the [O III] lines relative to Balmer lines, but these lines in RX J0439.6-5311 are also more blueshifted than those in 1H 0707-495. Note that if we adopt the NED redshift value of  $z = 0.243$ , RX J0439.6-5311 would exhibit significant blueshifts in all NLR and BLR lines relative to PG 1244+026, which is not likely to be correct.

#### 3.2 The NLR and BLR Outflows

AGN optical spectra often show abundant emission lines from both NLR and BLR, whose line profiles can be used to infer the physical properties and dynamics of these distinct emission line regions (e.g. Blandford & McKee 1982; Antonucci 1993; Peterson et al. 2014; Dopita et al. 2015). We performed a multi-gaussian line profile fitting to quantify the parameters of [O III] and H $\beta$  lines. Firstly, the Fe II lines were fitted between 4000-5500Å after subtracting a local continuum and masking out all other strong lines in



**Table 2.** The best-fit parameters for the line profiles of [O III] $\lambda$ 5007 and H $\beta$  (Fig. 2). Line-shift is relative to the vacuum wavelength, which is 5008.24Å for [O III] $\lambda$ 5007 and 4862.68Å for H $\beta$ , with negative values indicating blueshifts. Errors are for 1  $\sigma$  confidence level. EW is the equivalent width. An extra systematic uncertainty of  $\sim 300$  km s $^{-1}$  due to the redshift uncertainty should also be considered in all the line-shift measurements. NC is the narrow component in H $\beta$  with the same line profile as [O III] $\lambda$ 5007.

| Component              | Line-shift<br>(km s $^{-1}$ ) | FWHM<br>(km s $^{-1}$ ) | EW<br>(Å)      |
|------------------------|-------------------------------|-------------------------|----------------|
| [O III] $\lambda$ 5007 |                               |                         |                |
| Gaussian-1             | $-290 \pm 30$                 | $660 \pm 80$            | $2.0 \pm 0.4$  |
| Gaussian-2             | $-860 \pm 60$                 | $1940 \pm 70$           | $6.0 \pm 0.4$  |
| total                  | –                             | $1360 \pm 180$          | $8.0 \pm 0.6$  |
| H $\beta$              |                               |                         |                |
| Gaussian-1             | $150 \pm 20$                  | $440 \pm 60$            | $2.8 \pm 0.6$  |
| Gaussian-2             | $390 \pm 110$                 | $1340 \pm 140$          | $5.2 \pm 1.0$  |
| Gaussian-3             | $-860 \pm 70$                 | $7580 \pm 240$          | $20.4 \pm 0.5$ |
| NC                     | –                             | –                       | $0.6 \pm 0.3$  |
| total                  | –                             | $850 \pm 170$           | $29.0 \pm 1.3$ |

between. The Fe II template used in the fitting consists of the Fe II blends in I Zw 1 and four extra Fe II line groups (P, F, S, G), with the line-width and relative intensities determined by the fitting (Kovačević, Popović & Dimitrijević 2010; Shapovalova et al. 2012). After subtracting the best-fit Fe II template, we used multiple Gaussian components to fit the [O III] $\lambda$ 4959/5007 doublets and H $\beta$  line, simultaneously. The [O III] $\lambda$ 5007 line profile requires two gaussian components. [O III] $\lambda$ 4959 was assumed to have an identical profile as [O III] $\lambda$ 5007 with a fixed atomic flux ratio of 1:3. We also assumed that the narrow component of H $\beta$  line has the same profile as [O III] $\lambda$ 5007. Besides the narrow component, we found it necessary for H $\beta$  to have three extra Gaussian components: one fitting the narrow peak and two fitting the broad base. The fitting was performed using the MPFIT-EXPR program (Markwardt 2009) in the Interactive Data Language (IDL v8.4), and the results are shown in Fig. 2 and Table 2. The total FWHM of H $\beta$  was measured directly from the combined profile of best-fit Gaussian components excluding the narrow component, with its error determined by the Monte Carlo method. We point out that the redshift uncertainty of  $\sim 0.001$  corresponds to a velocity of 300 km s $^{-1}$ , which certainly affects the measurement of line-shift in every emission line.

From the line fitting results in Table 2, we find each of the [O III] double lines is dominated by a broad Gaussian component with FWHM =  $1940 \pm 70$  km s $^{-1}$ , blueshifted by  $860 \pm 60$  km s $^{-1}$  and comprises 75% of the total line flux, making the whole line profile very broad. This suggests that most of the NLR clouds emitting [O III] are outflowing. The fitting requires very little NLR component of the same profile as [O III] in the H $\beta$  line, but an extra component is required to fit the narrow peak of H $\beta$ . This suggests that the H $\beta$  NLR has different properties from the [O III] NLR. Then the broad base of H $\beta$  is dominated by a broad (FWHM =  $7580 \pm 240$  km s $^{-1}$ ) and blueshifted ( $v = -860 \pm 70$  km s $^{-1}$ ) component. The total H $\beta$  FWHM is only  $850 \pm 170$  km s $^{-1}$ , which is consistent with previous measurements (Grupe et

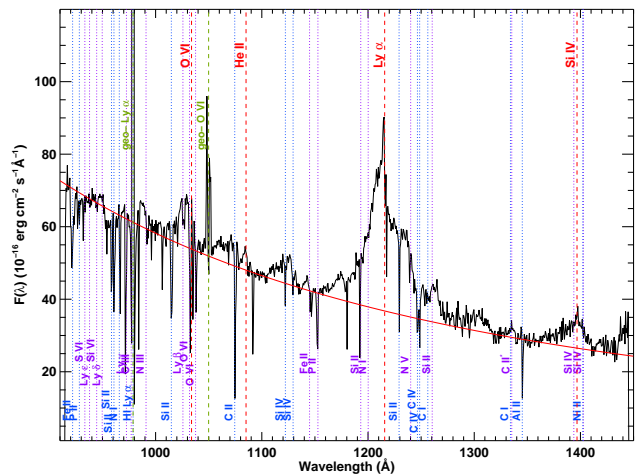


**Figure 3.** The combined *HST* COS spectrum (G130M + G160M) of RX J0439.6-5311, rebinned with 0.6 Å per bin to increase the S/N. The spectrum has been de-reddened for a Galactic reddening of  $E(B-V) = 0.013$  and de-redshifted for  $z=0.242$  to the AGN rest-frame. The red solid line is the best-fit power law to the continuum with  $\alpha = 2.35 \pm 0.02$ . Most of the absorption lines can be identified as Galactic absorption lines (blue) or host galaxy absorption lines (magenta). We also find two geo-coronal lines (dark green) and four emission lines (red) intrinsic to RX J0439.6-5311.

al. 2004a,b). Combining the results in Fig. 1 and 2, we can see that the BLR clouds in RX J0439.6-5311 show an outflow that is much stronger than in either PG 1244+026 or 1H 0707-495, suggesting a more powerful radiation field in RX J0439.6-5311. Compared to the strong blueshift in the NLR lines, only part of the H $\beta$  line profile is blueshifted, suggesting that the BLR clouds are likely optically thick, and so the radiation acceleration only causes an outflow in the lower density surface of the BLR clouds (Baskin, Laor & Stern 2014a).

### 3.3 Mapping the Accretion Flow in UV

For AGN with high mass accretion rates, their UV emission is often dominated by the emission from the outer accretion disc (hundreds of  $R_g$ ), and so the shape of the UV underlying continuum can be used to map the outer accretion flow. Fig. 3 shows the combined spectrum of RX J0439.6-5311 from all previous COS exposures (G130M & G160M) (Danforth et al. 2016). The spectrum extends down to 1120 Å in the observer's frame, or 900 Å in the rest-frame of RX J0439.6-5311, which corresponds to a radius of  $190 R_g$  in a standard accretion disc model (Shakura & Sunyaev 1973, hereafter: SS73) with  $M = 1 \times 10^7 M_\odot$  and  $\dot{m}_{\text{out}} \equiv \dot{M}_{\text{out}}/M = 5.9$  (see Section 6.1). There are many narrow absorption lines from the Milky Way and the host galaxy, as well as broad emission lines (Ly $\alpha$ , Si IV, He II, O VI) due to the AGN activity in RX J0439.6-5311. No broad absorption lines can be identified, which indicates a relatively small inclination angle and a clear line-of-sight to the accretion flow.

We used a power law ( $f_\lambda \propto \lambda^{-\alpha}$ ) to fit the underlying continuum after carefully masking out all strong emission and absorption lines, and found  $\alpha = 2.25 \pm 0.02$  before de-

reddening the spectrum. After applying the correction for the Galactic reddening of  $E(B - V) = 0.013$  (assuming  $E(B - V) = 1.7 \times 10^{-22} N_{\text{H}}$ , Bessell 1991) using the reddening curve of Milky Way in Pei (1992), the best-fit power law slope increases to  $\alpha = 2.35 \pm 0.02$  (Fig. 3, red solid line), which is fully consistent with the spectral slope of a standard thin disc model. Therefore, the unobscured UV continuum from *HST* COS clearly indicates the accretion flow in RX J0439.6-5311 behaves like a standard accretion disc down to  $190 R_{\text{g}}$  for the above mass and mass accretion rate. Previous studies of AGN composite UV spectra show a flatter spectral shape than a standard accretion disc spectrum at  $\lambda > 1000\text{\AA}$ , as well as an abrupt turnover at  $\sim 1000\text{\AA}$  (e.g. Zheng et al. 1997; Telfer et al. 2002; Shang et al. 2005; Barger & Cowie 2010; Shull, Stevans & Danforth 2012). We do not find any spectral shape change at  $1000\text{\AA}$  in RX J0439.6-5311 (Fig. 3), but we cannot rule out the existence of such a turnover below  $900\text{\AA}$ .

#### 4 BROADBAND SED ANALYSIS

A broadband SED can be used to constrain the accretion flow and measure the key parameters such as the bolometric luminosity and Eddington ratio (e.g. Jin et al. 2012a, Done et al. 2013; DJ16). In order to construct the broadband SED of RX J0439.6-5311, we make use of the combined *ROSAT* spectrum in the soft X-ray band, *XMM-Newton* EPIC-pn spectrum in the 0.3-10 keV band, *XMM-Newton* OM data in the UV/optical, continua measured from the combined *HST* spectrum and the single-epoch optical spectrum, as well as *WISE* and *2MASS* photometric points in the IR band. We imported all these data into XSPEC (v12.9.0o, Arnaud 1996) and performed the broadband SED fitting. The OPTXCONV model is used to model the broadband SED from optical to hard X-rays, which comprises an accretion disc component, a soft X-ray Comptonisation component and a hard X-ray Comptonisation component. The viewing angle effect and relativistic effects are also included in it (Done et al. 2013). Our detailed X-ray study in Paper-I shows that there could also be a weak reflection component, so we include a KDBLURXRFXCONVXNTHCOMP component in the model (see Paper-I for detailed explanations). The Galactic and intrinsic extinctions are both modelled with the TBNEW model using cross-sections of Verner et al. (1996) and interstellar medium (ISM) abundances of Wilms, Allen & McCray (2000). Galactic and intrinsic reddening are modelled with the (z)REDDEN model, assuming  $E(B - V) = 1.7 \times 10^{-22} N_{\text{H}}$  (Bessell 1991). The IR data are fitted with a hot dust template from Silva, Maiolino & Granato (2004). A Sa-type host galaxy template from the SWIRE library (Polletta et al. 2007) is also included to model the host galaxy starlight in the optical/UV band. We adopt  $z=0.242$ , an inclination angle of  $30^\circ$  and a zero spin for the SED fitting.

The normalisation discrepancy between non-simultaneous observations from different instruments is a major issue when fitting a broadband SED. This discrepancy consists of both aperture effect and variability of the source. RX J0439.6-5311 is a point-like source from IR to X-rays, so the aperture effect between different instruments is minimised. Regarding the variability issue, we have simultaneous optical/UV and X-ray data from

*XMM-Newton*. The *WISE* IR and *HST* UV observations are also nearly simultaneous (Table 1). RX J0439.6-5311 is also a high mass accretion rate QSO, which implies that its IR/optical/UV emission should be relatively stable (e.g. Ai et al. 2013; Meusinger & Weiss 2013). Therefore, the influence of source variability should also be small. We multiply a free scaling factor to the entire SED model to account for small normalisation discrepancies.

Our SED model produces a good fit to all the multi-wavelength data with  $\chi^2_{\nu} = 1089/712$  (Fig. 4). Small normalisation discrepancies are found relative to the *XMM-Newton* data, which is a factor of 1.31 for the *HST* spectra and IR data, 1.24 for the optical spectrum, and 0.97 for the *ROSAT* spectrum. The discrepancy in the optical/UV band would be smaller if we were able to correct for the contribution of emission line fluxes in the OM photometric points. However, because there was no simultaneous optical/UV spectra for the OM data, we have not attempted to do so. The soft and hard X-ray data are well fitted by the two Comptonisation components plus the weak reflection component, with the accretion disc component extending slightly into the soft X-ray band. No intrinsic extinction is required by the fitting ( $N_{\text{H}} < 10^{19} \text{cm}^{-2}$ ). These results are all consistent with our X-ray study in Paper-I. The optical/UV data are well fitted by the accretion disc spectrum without requiring any intrinsic de-reddening or a contribution from host galaxy star-light. The IR data are well fitted by the hot dust template alone. The fitting finds  $M = 1.8 \times 10^7 M_{\odot}$  and  $L/L_{\text{Edd}} = 1.8$  for a zero spin black hole. The corona radius  $R_{\text{cor}}$  is found to be  $29 R_{\text{g}}$ , within which all the disc energy is required to be dissipated into the two Comptonisation components. Although a better fit with  $\Delta\chi^2 = 7$  can be found for  $R_{\text{cor}} = 100 R_{\text{g}}$ , the disc component can no longer extend into the soft X-ray band for such a large  $R_{\text{cor}}$ , which is not consistent with our X-ray study discussed in Paper-I, therefore we rejected this fit. The hard X-ray Comptonisation contains 31% of the total Comptonisation energy and has a steep slope of  $\Gamma = 2.71$ . The soft X-ray Comptonisation has an electron energy of 0.25 keV and optical depth of 14.9, broadly consistent with the results in Paper-I.

The OPTXCONV model is self-consistent in terms of energy budget, although in the total SED model it does not include the energy in reflection which is very little. However, a major issue is that it does not include the energy lost due to a disc wind and/or advection, which mainly affects super-Eddington sources like RX J0439.6-5311 (Jin, Done & Ward 2016; DJ16). This means that OPTXCONV can over-estimate the disc luminosity at small radii, thereby producing a UV bump that is too strong when compared with the observations. Then the fitting will require an increase in the black hole mass in order to reduce the disc temperature and the strength of the UV bump, and so the best-fit black hole mass is then over-estimated. However, the assumption of zero spin can lead to an under-estimate of the black hole mass. For example, if we change the spin parameter to its maximal value of 0.998, the radiative efficiency increases to 0.321 (DJ16), and the UV bump becomes stronger and shifts to higher energy. Then the best-fit black hole mass increases to  $3.5 \times 10^7 M_{\odot}$  (i.e. up by a factor of 2 compared with that for zero spin) with an Eddington ratio of 2.2 in order to maintain a good fit. Although the true spin of RX J0439.6-5311 cannot be determined from the existing data, previ-

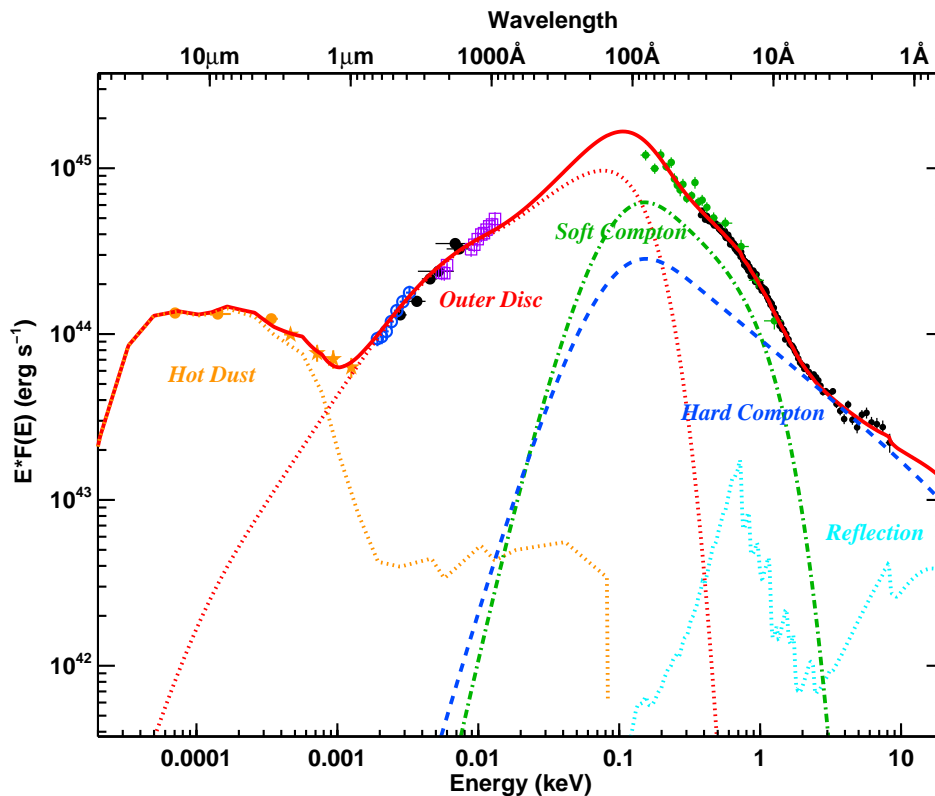


**Figure 4.** The broadband SED of RX J0439.6-5311, assuming an inclination angle of  $30^\circ$ . The data consist of *XMM-Newton* EPIC-pn spectrum and OM photometric points (black), a combined *ROSAT* spectrum (green points in the X-ray, scaled up by 3%), continual points from the *HST* COS spectra (magenta in the optical/UV, scaled down by 23%), the optical spectrum from Grupe et al. (2004a) (blue, scaled down by 20%), and the IR photometric points including WISE Band 1-4 (orange circles, scaled down by 23%) and 2MASS J, H, K (orange stars, scaled down by 23%). Red solid curve is the best-fit SED model, comprising an accretion disc component (red dotted curve), a soft X-ray Comptonisation component (green dash-dot curve), a hard X-ray Comptonisation component (blue dash-dot curve), a weak reflection component (cyan dotted curve) and a hot dust component (orange dotted curve). Note that this broadband SED model does not consider any energy loss due to the disc wind or advection.

ous studies show that SMBH with  $\sim 10^7 M_\odot$  may have a chaotic/episodic accretion history which leads to a low spin (e.g. King, Pringle & Hofmann 2008; Miniutti et al. 2009; Fanidakis et al. 2011; but see Orban de Xivry et al. 2011). So any bias caused by the assumption of zero spin may be smaller than that resulting from neglecting the presence of the disc wind and advection. Finally, we emphasise that the SED parameters reported above should be considered only as indicative for the intrinsic properties of the source, particularly noting that the mass is likely to be over-estimated (also see Section 6.1).

## 5 MULTI-WAVELENGTH VARIABILITY

### 5.1 Short-term Variability

By virtue of the unique capability of *XMM-Newton*, which allows the long and simultaneous observation in the X-ray and UV/optical bands with high time-resolution, the multi-wavelength short-term variability of RX J0439.6-5311 can be revealed clearly (Fig. 5). In Paper-I we have performed a full analysis of the short-term variability in the X-ray band and reported the Root-Mean-Square (RMS) fractional variability of  $22.4 \pm 0.4\%$ ,  $28.7 \pm 0.4\%$  and  $47.5 \pm 1.1\%$  in the 0.3-1, 1-2 and

2-10 keV bands, respectively. Compared to the strong X-ray variability, Fig. 5 shows that the optical/UV emission from RX J0439.6-5311 contains very little short-term variability. The intrinsic RMS variability is found to be  $10.7 \pm 5.8\%$  in UVW2, and is consistent with 0 in the other OM bands. We also searched for the covariance between UVM2 and X-rays light curves by calculating the cross-correlation function (CCF), but the variability in UVM2 is too small to allow any significant detection of UV/X-ray coherence or time-lag.

The SED in Fig. 4 shows that the flux contained in the soft X-rays is comparable to the flux in the optical/UV band, so if some of the highly variable soft X-rays illuminate the outer disc and are reprocessed as part of the disc emission, it may cause the optical/UV light curve to vary as well. This X-ray reprocessing mechanism has been proposed for many AGN in order to explain the commonly observed optical/UV reverberation lag in long-term monitoring campaigns of sub-Eddington AGN (e.g. Mason et al. 2002; Arévalo et al. 2005; Alston, Vaughan & Uttley 2013; Lohfink et al. 2014; Edelson et al. 2015; Buisson et al. 2017; but see Gardner & Done 2017). However, the short-term variability is more easily smeared in the outer disc, leading to a much weaker reverberation signal which is difficult to detect (Smith & Vaughan 2007; Robertson et al. 2015).

In order to understand how much variability is expected

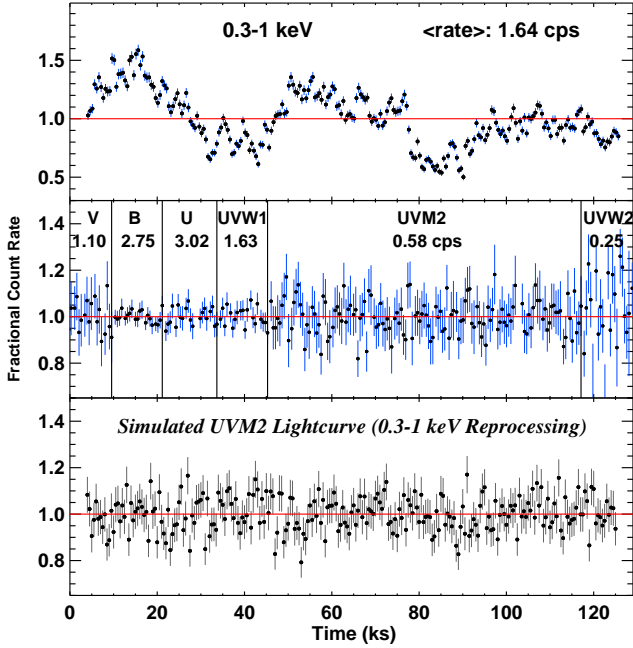


**Figure 5.** Short-term variability of RX J0439.6-5311 revealed by the 500 s binned, background subtracted light curves from EPIC-pn in the 0.3-1 keV band and the simultaneous exposures in the six OM bands. The labelled number indicates the mean source count rate in the unit of counts per second (cps). The bottom panel shows our simulation resulting from the reprocessing of the 0.3-1 keV light curve emerging in the UVM2 band, whose intrinsic RMS is only 0.22%.

in UVM2 if the soft X-rays within 0.3-1 keV is indeed reprocessed in the outer disc, we perform a simulation of this variability transmission using methods similar to those employed in Gardner & Done (2017). For the simulation we adopted a  $10^7 M_{\odot}$  black hole with a mass accretion rate of 5.9 (see Section 6.2). The soft X-ray source is located at  $30 R_g$  above the black hole on the spin axis (similar to the ‘lamp-post’ model geometry). The soft X-rays illuminate the outer disc, increasing the temperature and luminosity of every annulus. Then the emission from each annulus contains a constant disc component and a variable reprocessed component. The observed flux in UVM2 (bandpass:  $2310 \pm 240 \text{ \AA}$ , *XMM-Newton* Users Handbook) contains the emission from a range of annuli in the outer disc spanning hundreds of  $R_g$ . We use the PSD of 0.3-1 keV and the algorithm of Timmer & König (1995) to simulate more light curve segments, which are used as input for the simulation. The bottom panel of Fig. 5 shows the resultant UVM2 light curve with the same S/N as the real observation.

The suppression of reprocessed soft X-ray variability are mainly due to three causes. These include the dilution by the intrinsic UV disc emission, which can be considered as a stable component compared to the reprocessed component; the transfer function at each radius, which takes into account different light travel time to different azimuths at each radius; the wide outer disc region spanning hundreds of  $R_g$  that contributes significant flux in the UVM2 band with different light travel time (see Gardner & Done 2017). As a

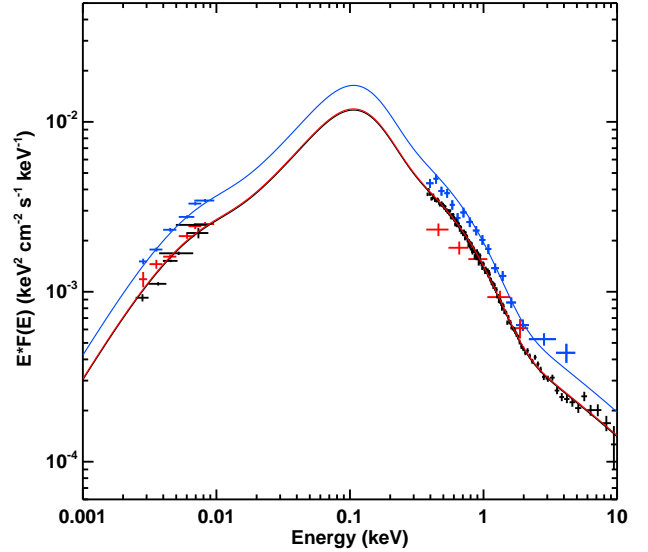


**Figure 6.** The long-term multi-wavelength variability of RX J0439.6-5311 revealed by *Swift* XRT/UVOT (blue: combined from four observations in 2006; red: combined from four observations in 2012 and 2014) and *XMM-Newton* EPIC-pn/OM (black: observed in 2016). The solid curves are the best-fit OPTXCONV models, with the blue model being 38% higher than the red model and 40% higher than the black model.

consequence, the simulated UVM2 light curve contains only 0.22% intrinsic RMS variability, which is hardly detectable with the given S/N. Adding the hard X-ray emission to the reprocessing cannot increase the UV variability significantly, because its luminosity is one order of magnitude less than that of the soft X-ray emission, and the reprocessed hard X-ray variability suffers similar suppression.

We also note that the above result does not depend on the input black hole mass or mass accretion rate. This is because a standard thin disc model has  $T^4 \propto M\dot{M}/R^3$  (SS73) and monochromatic luminosity below the disc peak of  $L_{\text{opt}} \propto (M\dot{M})^{2/3} \propto (M^2\dot{m})^{2/3}$  (Laor & Davis 2011, see also Section 6.2). Hence  $T \propto L_{\text{opt}}^{3/8} R^{-3/4}$  so that the radius in the disc which produces a given temperature is completely specified by the observed optical luminosity and does not depend on the model mass and mass accretion rate, hence the radius (e.g.  $\sim 670 R_g$  for  $M = 10^7 M_{\odot}$  and  $\dot{m} = 5.9$ ) which produces a temperature which peaks in the UVM2 band is completely defined by the data.

## 5.2 Long-term Variability

Although the short-term reprocessed X-ray variability cannot be detected in the outer disc emission, the fluctuation of mass accretion rate in the outer disc with much longer timescale can introduce a long-term variability, which may cause the accretion disc and corona emission to vary in a correlated pattern. RX J0439.6-5311 was monitored by the Catalina Survey from 2005-12-09 to 2012-12-18, and exhibited a factor of  $\sim 2$  variation in the V-band light curve, confirming the existence of a long-term variability in the outer disc.



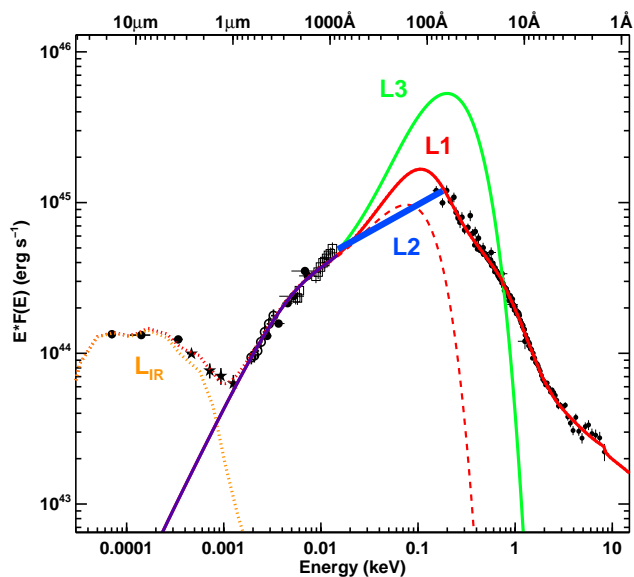


**Figure 7.** The same broadband SED as in Fig. 4. The red solid curve is the OPTXCONV plus reflection model with  $M = 1.8 \times 10^7 M_{\odot}$  and  $L_1/L_{\text{Edd}} = 1.8$  (the disc component is indicated by the red dash curve). An accretion disc spectrum of  $M = 7 \times 10^6 M_{\odot}$  and  $\dot{m} = 12.1$  is added to match the optical/UV flux (green solid curve, with a bolometric luminosity of  $L_3$ ), which clearly overshoots the soft X-ray data by a factor of up to 6.3. The thick blue line is a direct link from the UV data to the soft X-ray data, which provides a lower limit of the bolometric luminosity ( $L_2$ ).  $L_{\text{IR}}$  is the luminosity in the hot dust component (orange dotted curve). We find  $L_1 = 1.2L_2 = 0.4L_3 = 10.8L_{\text{IR}}$  (see Section 6.2).

The eight *Swift* observations of RX J0439.6-5311 between 2006 and 2014 (see Table 1), combined with our new *XMM-Newton* observation, provide the opportunity to test the long-term covariance between optical/UV and X-ray emission. However, all four observations obtained in 2006 show consistent fluxes, while the four observations in 2012 and 2014 also show similar flux but with low S/N due to the short exposure. Therefore, we combined the four observations in 2006 and the four observations in 2012-2014 to increase the S/N. The `addspec` and `fappend` tasks from `FTOOL` (v6.19) were used to combine the XRT spectra and UVOT exposures, separately. We took the best-fit OPTXCONV model in Fig. 4 and multiplied it by a free constant parameter to fit the two combined *Swift* SEDs in 2006 and 2012-2014. Fig. 6 shows that the best-fit SED model for the *XMM-Newton* data can also fit the *Swift* data simply by adjusting the normalisation. The SEDs observed by *Swift* in 2006 and 2012-2014 are a factor of  $1.40 \pm 0.02$  and  $1.02 \pm 0.02$  as luminous as observed by *XMM-Newton* in 2016, respectively. These results suggest a clear long-term covariance between the optical/UV disc emission and the X-ray corona emission, which is likely caused by the fluctuation of mass accretion rate in the outer disc. This fluctuation can change the luminosity of the accretion flow, but is probably not large enough to cause a significant change in the structure of the flow, and so it mainly affects the normalisation of the broadband SED rather than the overall shape.

## 6 DISCUSSION

### 6.1 Black Hole Mass Estimates

The black hole mass of a SMBH is often measured from single-epoch optical spectra (e.g. Vestergaard 2002; McLure & Jarvis 2002). For RX J0439.6-5311 Grupe et al. (2004a,b) measured the FWHM of  $H\beta$  line to be  $700 \pm 140 \text{ km s}^{-1}$  and derived a black hole mass of  $3.9 \times 10^6 M_{\odot}$  using the scaling relation reported by Kaspi et al. (2000). We revisit this black hole mass estimate using the results of our line fitting in Section 3 and applying more up-to-date scaling relations in the literatures.

Our  $H\beta$  line profile fitting gives a FWHM of  $850 \pm 170 \text{ km s}^{-1}$  (Table 2), which is broadly consistent with previous work. We notice that the partial blueshift in the  $H\beta$  line's base does not affect the FWHM of the line, because the FWHM is mainly determined by the two narrower components (see Fig. 2). The flux measured at the rest-frame  $5100\text{\AA}$  is  $2.96 \times 10^{-16} \text{ erg cm}^{-2} \text{ s}^{-1} \text{ \AA}^{-1}$ . With a luminosity distance of 1187.1 Mpc (Wright 2006) and assuming an isotropic source, we find the monochromatic luminosity at  $5100\text{\AA}$  to be  $L_{5100} = 2.55 \times 10^{44} \text{ erg s}^{-1}$ . Then the black hole mass is estimated to be  $9.4 \times 10^6 M_{\odot}$  using the Vestergaard & Peterson (2006) (VP06) relation or  $6.7 \times 10^6 M_{\odot}$  using the Woo & Urry (2002) (WU02) relation. These mass estimates typically have a  $1\sigma$  systematic uncertainty of  $\sim 0.5$  dex. If we use the Marconi et al. (2010) (M08) scaling relation to correct for the radiation pressure within the BLR, the black hole mass would increase to the value of  $1.0 \times 10^8 M_{\odot}$ . If we assume an inclination angle of  $30^\circ$  rather than isotropic,  $L_{5100}$  reduces to  $1.47 \times 10^{44} \text{ erg s}^{-1}$ , then the black hole mass reduces to  $7.1 \times 10^6 M_{\odot}$  for the VP06 relation,  $4.6 \times 10^7 M_{\odot}$  for the WU02 relation, and  $5.9 \times 10^7 M_{\odot}$  for the M08 relation. But it has been reported that the M08 relation is likely to over-estimate the black hole mass, because the weakly ionised BLR clouds are like to be optically thick as suggested by the  $H\beta$  line profile (see Section 3), and so the radiation pressure can only affect the surface of the BLR rather than dominating the entire region (Baskin, Laor & Stern 2014b).

Another independent black hole mass estimate can be obtained using the correlation between the black hole mass and the hard X-ray variability, regardless of the details about the variability mechanism (Miniutti et al. 2009; Zhou et al. 2010; Ponti et al. 2012; Ludlam et al. 2015; Jin, Done & Ward 2016). The 2-10 keV excess variance ( $\sigma_{\text{rms}}^2$ ) of RX J0439.6-5311 is  $0.078 \pm 0.007$  for the 250s-binned 40 ks light curve segments from the *XMM-Newton* observation; while for a 80 ks light curve segment, we find  $\sigma_{\text{rms}}^2 = 0.086 \pm 0.008$  (Vaughan et al. 2003). Using the scaling relations in Ponti et al. (2012), the black hole mass is estimated to be  $2 \times 10^6 M_{\odot}$ . Jin, Done & Ward (2016) revisited this relation using a more complete reverberation mapping sample and presented the regression results, from which we can derive a  $2\sigma$  range of  $0.5\text{--}8.0 \times 10^6 M_{\odot}$  for the black hole mass.

In addition, we can also obtain a rough estimate of the black hole mass from the scaling relation between the mass, bolometric luminosity and high frequency break in the X-ray PSD (McHardy et al. 2007). Adopting a high frequency break of  $6.4_{-2.7}^{+4.7} \times 10^{-4} \text{ Hz}$  as being observed in the 0.3-1 keV PSD (see Paper-I), and a bolometric luminosity of  $4.2 \times 10^{45} \text{ erg s}^{-1}$  (see next section), the black hole mass is found to

**Table 3.** Comparison of the mass accretion rate through the outer disc ( $\dot{m}_{\text{out}}$ ) and the observed Eddington ratio ( $L_{\text{bol}}/L_{\text{Edd}}$ ) for  $L_1$  and  $L_2$  in Fig. 7. We assume  $30^\circ$  inclination angle and zero spin. A higher spin or a larger inclination angle will further increase the  $\dot{m}_{\text{out}}$  values (see DJ16).

| BH Mass ( $M_\odot$ )  | $5 \times 10^6$ | $7 \times 10^6$ | $1 \times 10^7$ | $1.8 \times 10^7$ |
|------------------------|-----------------|-----------------|-----------------|-------------------|
| $L_1/L_{\text{Edd}}$   | 6.5             | 4.6             | 3.2             | 1.8               |
| $L_2/L_{\text{Edd}}$   | 5.4             | 3.8             | 2.7             | 1.5               |
| $\dot{m}_{\text{out}}$ | 23.8            | 12.1            | 5.9             | 1.8               |

be  $4.3^{+1.3}_{-1.0} \times 10^6 M_\odot$ . Therefore, despite the low significance, the high frequency break in the 0.3-1 keV PSD also indicates a black hole mass within the  $2\sigma$  range from the X-ray variability method.

Considering all the above black hole mass estimates, as well as the mass of  $1.8 \times 10^7 M_\odot$  derived from the SED fitting in Section 4 which is most likely to be an over-estimate, a reasonable estimate of the black hole mass of RX J0439.6-5311 is likely to be  $5 - 10 \times 10^6 M_\odot$ , which is slightly larger than the SMBH in PG 1244+026 (J13) and 1H 0707-495 (DJ16).

## 6.2 Bolometric Luminosity and Mass Accretion Rate

The well-constrained SED of RX J0439.6-5311, together with the low Galactic and intrinsic extinction, enables us to make one of the most reliable estimates of an AGN bolometric luminosity. Using  $M = 1.8 \times 10^7 M_\odot$  and  $L_{\text{bol}}/L_{\text{Edd}} = 1.8$  based on the best-fit SED with zero spin, we can derive a bolometric luminosity of  $L_{\text{bol}} = 4.2 \times 10^{45} \text{ erg s}^{-1}$  for a  $30^\circ$  inclination angle<sup>4</sup> ( $L_1$  in Fig. 7). This SED model predicts a peak in emission between 100-150 Å where no data exist, and so  $L_1$  will contain some uncertainty. Therefore, we calculate a more conservative  $L_{\text{bol}}$  by simply linking the UV data to the soft X-ray data and integrating the luminosity below it (i.e.  $L_2$  in Fig. 7). We find  $L_2 = 3.5 \times 10^{45} \text{ erg s}^{-1} = 0.83L_1$ , which can be considered as a lower limit for the true  $L_{\text{bol}}$ .  $L_1$  can be considered as an upper limit because it does not consider any other forms of energy loss in the disc (see Section 6.3).

The well-constrained  $L_{\text{bol}}$  also allows us to accurately measure the bolometric corrections at 5100 Å ( $k_{5100} \equiv L_{\text{bol}}/L_{5100}$ ) and the 2-10 keV band ( $k_{2-10} \equiv L_{\text{bol}}/L_{2-10 \text{ keV}}$ ). We find  $k_{5100} = 37$  and 31,  $k_{2-10} = 91$  and 76 for  $L_1$  and  $L_2$ , respectively. These values are significantly larger than the commonly adopted values (e.g. Kaspi et al. 2000:  $k_{5100} = 9$ ; Richards et al. 2006:  $k_{5100} = 10.3$ ), but are consistent with reported correlations between various bolometric corrections and Eddington ratio (Vasudevan & Fabian 2007, 2009; Jin, Done & Ward 2012c). The reason for this Eddington ratio dependence is that the broadband SED contains a much

<sup>4</sup> The best-fit *maximal-spin* SED model gives  $M = 3.5 \times 10^7 M_\odot$  and  $L_{\text{bol}}/L_{\text{Edd}} = 2.2$ , which would then increase  $L_1$  by a factor of 2.4. This is because the maximal-spin SED contains a stronger peak than the zero-spin SED in the unobservable far-UV band. But this black hole mass is too large compared to the other mass estimates in Section 6.1, so the maximal-spin SED is not adopted in our further analysis.

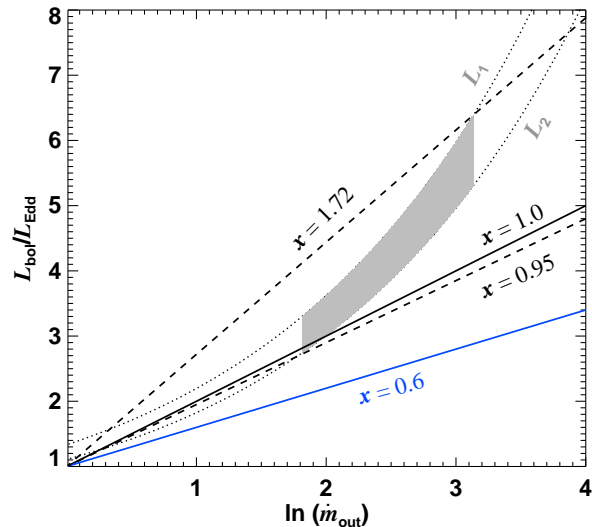


**Figure 8.** Constraining the  $\alpha$  factor in the relation  $L_{\text{bol}}/L_{\text{Edd}} = 1 + x \ln(\dot{m}_{\text{out}})$ . The two dotted curves indicate the  $L_{\text{bol}}/L_{\text{Edd}}$  vs.  $\ln(\dot{m}_{\text{out}})$  relation for the observed optical/UV flux and the  $L_{\text{bol}}$  limits of  $L_1$  and  $L_2$  in Fig. 7. The grey region is defined by  $L_2 \leq L_{\text{bol}} \leq L_1$  and  $5 \times 10^6 M_\odot \leq M \leq 1.0 \times 10^7 M_\odot$ .  $x = 1$  (black solid line) and 0.6 (blue solid line) are predicted by the super-Eddington disc models considering only advection and outflow, respectively (see Poutanen et al. 2007). The two black dash lines indicate the range of  $\alpha$  as constrained by the grey region.

stronger big blue bump when the black hole mass is lower and the mass accretion rate is higher, thereby producing much larger bolometric corrections. Therefore, the results in this paper highlight the importance of using the Eddington ratio dependent bolometric corrections as given in e.g. Vasudevan & Fabian (2009) and Jin, Done & Ward (2012c), or alternatively by using the broadband SED to derive  $L_{\text{bol}}$  directly.

Now we can use  $L_1$  and  $L_2$  to estimate the Eddington ratio for different black hole masses using  $L_{\text{bol}}/L_{\text{Edd}} \propto M^{-1}$  for a fixed  $L_{\text{bol}}$ . We can also estimate the mass accretion rate through the outer disc (hereafter:  $\dot{m}_{\text{out}}$ ) using the optical/UV luminosity ( $L_{\text{opt}}$ ) and the relation  $L_{\text{opt}} \propto (M^2 \dot{m}_{\text{out}})^{2/3} \cos i$ , where  $i$  is the inclination angle (Davis & Laor 2011; DJ16). Table 3 compares  $L_{\text{bol}}/L_{\text{Edd}}$  with  $\dot{m}_{\text{out}}$  for a range of black hole masses, and shows that  $\dot{m}_{\text{out}}$  is clearly much larger than  $L_{\text{bol}}/L_{\text{Edd}}$  if the black hole mass is  $\lesssim 10^7 M_\odot$ . This strongly suggests that the accretion flow loses gravitational energy through physical processes other than radiation, the details of which are discussed in the next section.

## 6.3 Energy Loss through the Disc Wind and Advection

The SS73 standard accretion disc model can be applied when the gravitational energy of the disc material is fully thermalised and dissipated as radiation. In the case of a super-Eddington source ( $\dot{m}_{\text{out}} > 1$ ) such as RX J0439.6-5311, the accretion flow is radiation pressure supported and is both geometrically and optically thick. In this case both advection and disc wind can carry away significant amount of disc energy, thereby reducing the energy radiated (e.g.

SS73; Abramowicz et al. 1988; Lipunova 1999; Poutanen et al. 2007; Ohsuga & Mineshige 2011; Takeuchi et al. 2014; Laor & Davis 2014; Jiang, Stone & Davis 2014; Sądowski & Narayan 2015; Hashizume et al. 2015; Hagino et al. 2016; DJ16). In Fig. 7, the green curve shows a standard accretion disc spectrum with  $M = 7 \times 10^6 M_\odot$  and  $\dot{m}_{\text{out}} = 12.1$  in order to reproduce the observed optical/UV flux. This model clearly over-predicts the soft X-ray emission, with the largest discrepancy being a factor of 6.3. The Eddington ratio for  $L_1$  is only 4.6 (i.e. 38%  $\dot{m}_{\text{out}}$ ). Similar discrepancies have been found in other sources like PG 1244+026, 1H 0707-495 (DJ16), and is probably most severe in the intermediate mass black hole (IMBH) RX J1140.1+0307 (Jin, Done & Ward 2016). All these sources have a  $\dot{m}_{\text{out}}$  that significantly exceeds the Eddington limit, suggesting that extra energy loss through a disc wind and/or advection exist in many super-Eddington sources.

Fig. 7 shows that the discrepancy between a standard disc model and the data only exists in the far-UV and soft X-ray band, while Fig. 3 shows that the optical and near-UV spectrum is consistent the standard disc model. These results clearly indicate that a disc wind and/or advection only occurs within some critical radii, where the accretion flow starts to behave differently from a standard thin disc. Understanding the structure and physical properties of these extreme accretion flows requires detailed hydrodynamic simulations (e.g. Ohsuga et al. 2005; Okuda et al. 2005; Jiang, Stone & Davis 2013; Jiang, Davis & Stone 2016). Nevertheless we can gain a basic understanding of these flows by using simplified analytical calculations. In the case of a super-Eddington disc with advection (i.e. the so-called ‘slim’ disc, Abramowicz et al. 1988), the critical radius ( $R_{\text{crit}}$ ) is where the photon escape time-scale is equal to the accretion time-scale. It has been found that  $R_{\text{crit}} \approx \dot{m}_{\text{out}} R_{\text{in}}$ , where  $R_{\text{in}}$  is the inner radius, and  $L_{\text{bol}}/L_{\text{Edd}} = 1 + \ln(\dot{m}_{\text{out}})$  (Watarai et al. 2000; Pounanen et al. 2007). In the case of a super-Eddington disc with a disc wind,  $R_{\text{crit}}$  is where the half-thickness of the disc is equal to the radius (SS73; Bisnovaty-Kogan & Blinnikov 1977; Lipunova 1999), then  $R_{\text{crit}} \approx \dot{m}_{\text{out}} R_{\text{in}}$  and  $L_{\text{bol}}/L_{\text{Edd}} = 1 + 0.6 \ln(\dot{m}_{\text{out}})$  (Pounanen et al. 2007). Numerical simulations show that both advection and disc wind can exist in a super-Eddington accretion flow (e.g. Eggum, Coroniti & Katz 1988; Ohsuga et al. 2005; Okuda et al. 2005), in which case Pounanen et al. (2007) shows that  $R_{\text{crit}}$  has a weak dependence on the relative strength between the advection and the disc wind (their Equation 21).

Given its well constrained  $L_{\text{bol}}$  and  $L_{\text{opt}}$ , RX J0439.6-5311 offers a great opportunity to test these theoretical results. The main uncertainty lies in the black hole mass. Since  $L_{\text{bol}}/L_{\text{Edd}}$  and  $\dot{m}_{\text{out}}$  both depend on the black hole mass, we can derive a relation between these two parameters for  $L_1$  and  $L_2$  (i.e. the two dotted curves in Fig. 8). We can further constrain this relation by adopting a black hole mass range of  $5 - 10 \times 10^6 M_\odot$  (the grey region in Fig. 8). For the relation  $L_{\text{bol}}/L_{\text{Edd}} = 1 + x \ln(\dot{m}_{\text{out}})$ , the difference between advection and a disc wind lies in the  $x$  factor, which is 1.0 for only advection and 0.6 for only disc wind. Fig. 8 shows that  $x = 0.6$  under-estimates  $L_{\text{bol}}/L_{\text{Edd}}$  for a specific  $\dot{m}_{\text{out}}$ , while  $x = 1.0$  is roughly consistent with  $L_{\text{bol}} \sim L_2$  and  $M \sim 10^7 M_\odot$ . The grey region constrains  $x$  to be  $0.95 \leq x \leq 1.72$ , with a larger  $x$  indicating a higher  $L_{\text{bol}}$  and a lower  $M$ . Therefore, our results suggest that the super-Eddington accretion flow in RX

**Table 4.** The distance of the soft X-ray excess ( $R_{\text{SX}}$ ) measured from the LF time lag ( $\tau_{\text{LF}}$ ) in RX J0439.6-5311, PG 1244+026 (Jin, Done & Ward 2013; Alston, Done & Vaughan 2014), RE J1034+396 (Middleton et al. 2009; Kara et al. 2016) and RX J1140.1+0307 (Jin, Done & Ward 2016).  $\dot{m}_{\text{out}}$  is the mass accretion rate measured from the optical/UV flux for the adopted black hole mass and zero spin.  $R_{\text{hump}}$  is the radius in a standard thin disc corresponding to  $\sim 1.8 \times 10^5 \text{ K}$ , where an iron opacity hump can exist to produce a puffed-up disc region (Jiang, Davis & Stone 2016) .

| Source   | BH Mass<br>( $10^6 M_\odot$ ) | $\dot{m}_{\text{out}}$ | $\tau_{\text{LF}}$<br>(ks) | $R_{\text{SX}}$<br>( $R_g$ ) | $R_{\text{hump}}$<br>( $R_g$ ) |
|----------|-------------------------------|------------------------|----------------------------|------------------------------|--------------------------------|
| RX J0439 | 10                            | 5.9                    | $3.4 \pm 0.8$              | $70 \pm 16$                  | 40                             |
| PG 1244  | 2                             | 13                     | $0.5 \pm 0.3$              | $50 \pm 30$                  | 90                             |
| RE J1034 | 2                             | 2                      | $1.6 \pm 0.8$              | $160 \pm 80$                 | 50                             |
| RX J1140 | 1                             | 10                     | $0.6 \pm 0.3$              | $120 \pm 60$                 | 110                            |

J0439.6-5311 tends to radiate more energy than predicted by the theoretical calculations for accretion disc models with advection and a disc wind.

In addition, assuming  $R_{\text{in}} = 6 R_g$  and using Equation 12 in Pounanen et al. (2007),  $R_{\text{crit}}$  can be calculated to be  $140 - 170 R_g$ ,  $70 - 82 R_g$  and  $33 - 36 R_g$  for  $M = 5 \times 10^6 M_\odot$ ,  $7 \times 10^6 M_\odot$  and  $1 \times 10^7 M_\odot$ , respectively. These  $R_{\text{crit}}$  values all indicate that the SED flattening due to the disc wind and advection should emerge at  $\lambda < 900 \text{ \AA}$ , which is consistent with the SED shown in Fig. 7. However, we cannot further constrain  $R_{\text{crit}}$  from current observations due to the lack of data in the unobservable far-UV region.

#### 6.4 Connection between the Soft X-ray Region and the Puffed-up Inner Disc Region

A geometrically thick inner disc region in a super-Eddington accretion flow is predicted by theoretical calculations (e.g. Abramowicz et al. 1988; Wang & Netzer 2003; Ohsuga & Mineshige 2011), and supported by three-dimensional Magnetohydrodynamics (MHD) simulations of super-Eddington accretion discs (e.g. Jiang, Davis & Stone 2014; Sądowski et al. 2014), and required by observations to explain the weak optical/UV emission lines (e.g. C IV, He II, [O III]  $\lambda 5007$ ) in radio-quiet weak emission-line quasars (WLQs) which are accreting near/above their Eddington limits (e.g. Boroson & Green 1992; Baskin & Laor 2004; Shen & Ho 2014; Shemmer & Lieber 2015). Moreover, in WLQs it was also suggested that for the disc shielding mechanism to work efficiently to produce weak NLR and BLR lines, the puffed-up region has to be high enough and the X-ray corona region has to be compact ( $\sim 10 R_g$ , Luo et al. 2015 and references therein). However, these conditions are difficult to meet in NLS1s, especially for those with super-Eddington mass accretion rates and weak [O III] lines relative to Balmer lines (e.g. Jin et al. 2012a). This is because in sources like RX J0439.6-5311 and PG 1244+026 the distance from the SMBH to the soft X-ray region is at least tens of  $R_g$  (estimated from the light travel time), and the soft X-ray region radiates much more energy than the hard X-ray region. Furthermore, Jin, Ward & Done (2012b) showed that [O III]  $\lambda 5007$  exhibits a much stronger correlation with the hard X-rays than with the soft X-rays. These results suggest that the NLR clouds can ‘see’

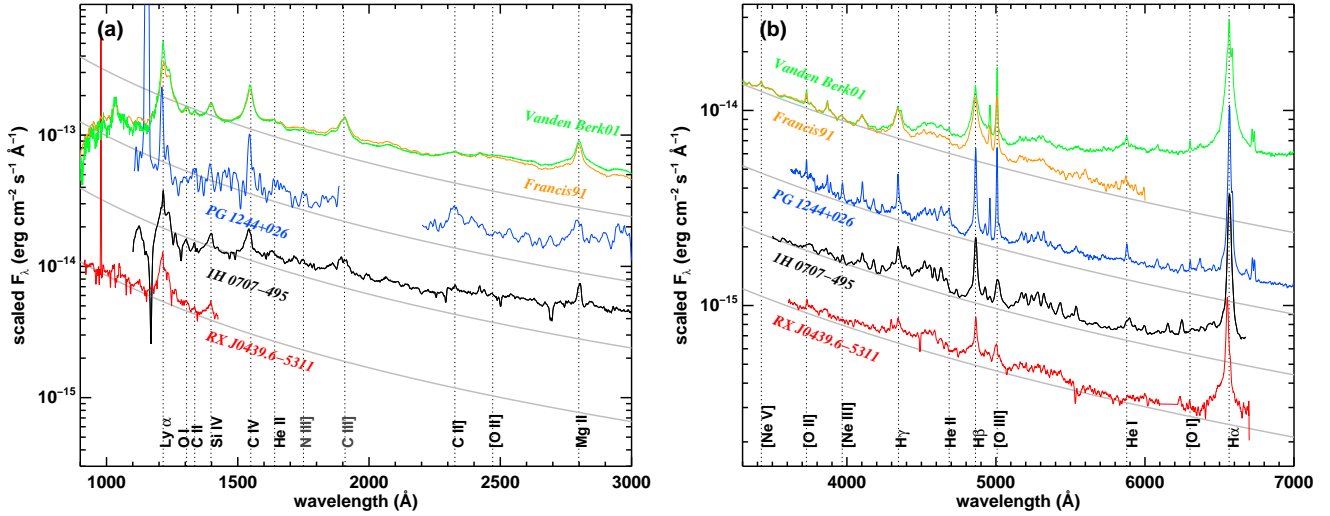


**Figure 9.** Comparison of the rest-frame optical/UV continua and emission lines between RX J0439.6-5311 (red), PG 1244+026 (blue), 1H 0707-495 (black), the bright quasar composite spectrum from Francis et al. (1991) (orange) and the SDSS quasar composite spectrum from Vanden Berk (2001) (green). Panel-a shows the comparison in the UV band, including the IUE spectra of PG 1244+026 and combined *HST* spectra of RX J0439.6-5311 and 1H 0707-495. Panel-b shows the comparison in the optical band, including the SDSS spectrum of PG 1244+026, ESO optical spectrum of RX J0439.6-5311 and CTIO spectrum of 1H 0707-495 (see DJ16). Each of the grey curves indicates the continuum shape predicted by a standard thin disc rescaled to the flux level of each spectrum. Galactic reddening has been corrected for the three individual sources. The flux of PG 1244+026 and 1H 0707-495 have been rescaled for clarity, while the flux of RX J0439.6-5311 is not changed.

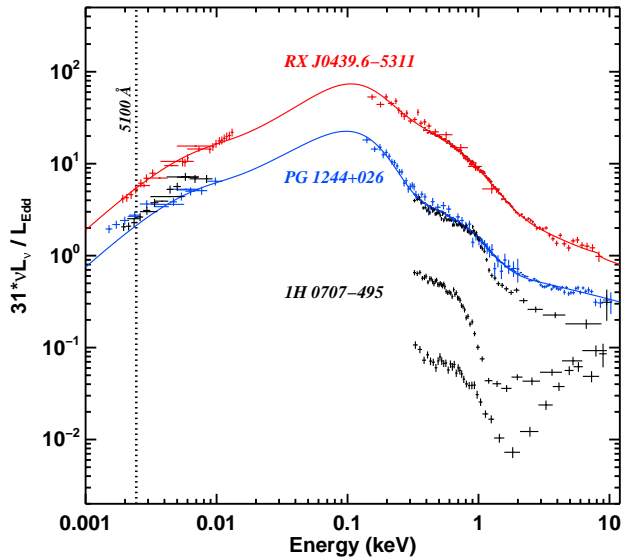


**Figure 10.** Comparison of the rest-frame broadband SED between RX J0439.6-5311 (red), PG 1244+026 (blue) and 1H 0707-495 (black). All the SEDs have been rescaled to show the Eddington ratio at 5100Å with a bolometric correction of  $k_{5100} = 31$  (see Section 6.2). The three X-ray spectra of 1H 0707-495 represent three typical spectral shape of this source (see DJ16). A host galaxy component is not included in the SED of PG 1244+026 (see J13), and is not required in the other two sources.

the nuclear hard X-ray emission, but is shielded from the soft X-ray emission.

Recently, Jiang, Davis & Stone (2016) applied their three-dimension MHD simulation of accretion disc around

a SMBH to show that the iron opacity bump due to the bound-bound transition of Fe can increase the stability of the disc, change the disc structure and drive an outflow. Since this opacity bump only exists around  $1.8 \times 10^5$  K and is sensitive to the temperature, it only creates a puffed-up disc structure at a certain radial distance. For the ‘simple’ NLS1s mentioned above, we can make a rough comparison between the radius of the soft X-ray region ( $R_{\text{SX}}$ ) and the radius of the  $1.8 \times 10^5$  K disc region ( $R_{\text{hump}}$ ). These radii depend on the black hole mass, mass accretion rate and the temperature structure of the super-Eddington accretion flow. Since each of these factors contains significant uncertainty, we can only expect to obtain an order-of-magnitude estimate. We use the time-lag between the soft and hard X-rays below  $10^{-4}$  Hz to estimate the distance between the soft and hard X-ray corona (Paper-I), which is probably only a lower limit due to the multi-component dilution effect, while a more realistic measurement would require a full spectral-timing analysis which is then model-dependent (Gardner & Done 2014). Then we use the temperature structure of a standard thin disc to estimate  $R_{\text{hump}}$ , which is also likely to be a lower limit. This is because the effective disc temperature would be much higher for low mass and high mass accretion rate when the vertical disc structure is taken into consideration (e.g. Davis & Hubeny 2006; Done & Davis 2008; Done et al. 2012). However, since the outer part of a super-Eddington accretion disc is likely to remain as a standard thin disc (e.g. Davis & Laor 2011), this estimate may still be roughly valid. In any case the uncertainty in black hole mass can easily introduce a factor of a few uncertainty to both  $R_{\text{SX}}$  and  $R_{\text{hump}}$ .

Despite all potential uncertainties, we find that  $R_{\text{SX}}$  is roughly consistent with  $R_{\text{hump}}$  (Table 4), which indicates the possible connection between the soft X-ray region and the



puffed-up disc region. The inner edge of the puffed-up disc region might be highly ionised and so could provide the low temperature, optically thick electrons required to produce the soft excess, as being described in Paper-I. This geometry naturally produces a large covering factor for the outer disc and emission line regions to be sufficiently shielded from the luminous soft X-ray region, without requiring the disc to be highly puffed-up or the X-ray emitting region to be very compact. Furthermore, in Paper-I we showed that the soft X-ray region provides seed photons for the hard X-ray corona. As  $R_{\text{SX}}$  increases with  $\dot{m}_{\text{out}}$ , its covering factor for the hard X-ray corona may decrease, which then provides a possible explanation for the observed weaker hard X-ray emission in higher mass accretion sources (e.g. the strong correlation between  $K_{2-10}$  and  $L_{\text{bol}}/L_{\text{Edd}}$ , Vasudevan & Fabian 2007, 2009; Jin, Done & Ward 2012c).

Finally, Paper-I showed that the soft excess in RX J0439.6-5311 is very smooth and so it does not favour any line features as would be present in the reflection spectrum modelled with RFXCONV. Even if the soft X-ray is modelled with the soft X-ray Comptonisation plus a weak disc reflection, a small  $R_{\text{in}}$  of  $2.80^{+2.74}_{-1.80}$  is still required to introduce sufficient relativistic smearing to the line features in the reflection component (see Figure 5 in Paper-I). However, we notice that the RFXCONV model is essentially based on the assumption of a constant-density atmosphere above the accretion disc (Ross & Fabian 2005 and references therein), but the puffed-up disc region is more likely to be in the hydrostatic pressure equilibrium state. Done & Nayakshin (2007) have shown that the soft excess in the hydrostatic models is much weaker than in the constant-density model, thus the reflection spectrum from the puffed-up disc region may be more smooth in the soft X-ray band, thereby relaxing the requirement for a very small  $R_{\text{in}}$  (or a very high black hole spin).

### 6.5 A Unified Picture for the Accretion Flow in ‘Simple’ and ‘Complex’ Super-Eddington NLS1s

DJ16 has shown that PG 1244+026 and 1H 0707-495 have similar black hole masses and mass accretion rates, and so their accretion flows may have similar properties. Then the apparent differences in their X-ray spectra can be explained as due to different viewing angles relative to the clumpy disc wind. However, a remaining problem is that their optical emission lines are very different from each other, with PG 1244+026 having much stronger NLR lines than 1H 0707-495. If the viewing angle scenario is correct, there should be some NLS1s with similar optical/UV emission lines to 1H 0707-495 and similar broadband SED shape to PG 1244+026. We find RX J0439.6-5311 is indeed such a source.

Firstly, we compare these three NLS1s in terms of their optical/UV spectra. PG 1244+026 has IUE and SDSS spectra, while 1H 0707-495 has *HST* STIS spectra and an optical spectrum from the Cerro Tololo Inter-American Observatory (CTIO). Since these spectra were not observed simultaneously, we perform the comparison in optical and UV band, separately. In addition, we include the bright quasar composite spectrum from Francis et al. (1991) and SDSS quasar composite spectrum from Vanden Berk (2001). In Fig. 10a,b

we can clearly see that RX J0439.6-5311 and 1H 0707-495 have very similar optical/UV spectra, implying similar intrinsic SEDs. Compared with the quasar composite spectra, these two sources have much weaker [O III] $\lambda$ 4959/5007 doublets whose ionisation potential is 55 eV, but some other lines of similar ionisation potentials such as C IV (64 eV) and Si IV (45 eV) have similar equivalent widths. Reverberation mapping studies have shown that C IV and Si IV emission line regions are much closer to the black hole than H $\beta$  and [O III] (e.g. Zu, Kochanek & Peterson 2011; Peterson et al. 2014), thus these elements may still ‘see’ the ionising source in the nuclear. Therefore, the optical/UV emission lines also depend on their location relative to the black hole and accretion disc. The NLR lines in PG 1244+026 are stronger than those seen in the quasar composite spectra which are dominated by the AGN emission, and so is consistent with the possibility that some of the narrow line emission in PG 1244+026 may come from an extended NLR region (ENLR) where ionisation by young massive stars in the host galaxy is likely to dominate (Unger et al. 1987; Husemann et al. 2014).

We notice that the spectra of PG 1244+026 and 1H 0707-495 and the two quasar composite spectra all appear flatter than the standard thin disc model. Since we only corrected for the Galactic reddening for the three NLS1s, part of this flatness might be due to some intrinsic reddening, especially for the two composite spectra. The presence of some contribution from a host galaxy can also produce a flattening in the optical-UV continuum, which is most likely in PG 1244+026 and 1H 0707-495 whose host galaxies can be resolved. However, RX J0439.6-5311 is an AGN at  $z=0.242$  with no detectable intrinsic reddening, and so it is not affected by the host galaxy star-light or reddening. This is also consistent with the fact that its optical/UV continuum is most consistent with a standard disc. Reprocessing occurring within the disc could also contribute to the continuum flattening, but it is difficult to quantify without simultaneous optical and UV spectra.

We also compare the broadband SED from optical to hard X-ray bands among these three NLS1s. DJ16 conducted a detailed comparison of the broadband SED between PG 1244+026 and 1H 0707-495. They reported that for the same black hole mass of  $2 \times 10^6 M_{\odot}$ ,  $30^{\circ}$  inclination angle and zero spin, both sources have  $\dot{m}_{\text{out}} \gtrsim 10$ . 1H 0707-495 is  $\sim 50\%$  more luminous than PG 1244+026 in the optical/UV band, but is always fainter than PG 1244+026 in the X-ray band with two orders of magnitude variability. Now we add RX J0439.6-5311 to this comparison by rescaling the SED by a factor of  $k_{5100} = 31$  (Section 6.2), so that the y-axis value at  $5100\text{\AA}$  directly indicates the Eddington ratio. Fig. 10 shows that RX J0439.6-5311 has a very similar broadband SED to PG 1244+026, except that it is a factor of 3 more super-Eddington.

Summarising all the above comparison, we find that RX J0439.6-5311 has similar optical/UV spectra to 1H 0707-495 and similar SED to PG 1244+026, thereby providing good evidence that ‘simple’ and ‘complex’ super-Eddington NLS1s can indeed be unified in the inclination angle scenario as shown in Fig. 11. Both RX J0439.6-5311 and PG 1244+026 have low inclination angles with clear line-of-sights directly to the core region. But 1H 0707-495 has a larger inclination angle, and so the disc wind material can

intervene in the line-of-sight to the nuclear region, thereby absorbing X-rays and introducing extra X-ray variability.

### 6.6 Super-Eddington NLS1s as the Low-redshift Analogs of Weak Emission-line Quasars

We compare the super-Eddington NLS1s with the radio-quiet WLQs at high redshifts. WLQs are well-known for their weak UV/optical high ionisation lines and prominent UV Fe II and Fe III emission (e.g. Diamond-Stanic et al. 2009; Plotkin et al. 2010a,b; Wu et al. 2012; Luo et al. 2015 and references therein). PHL 1811 is one of the most extreme and best studied WLQ, whose optical/UV spectra show little forbidden or semi-forbidden lines (e.g. Leighly et al. 2007). It has been suggested that WLQs can be divided into two subtypes according to their X-ray luminosity, about half of WLQs are X-ray normal, while the other half are X-ray weak (including PHL 1811 and its analogs, e.g. Shemmer et al. 2009; Wu et al. 2012; Luo et al. 2015). The spectral stacking results in Luo et al. (2015) indicate that the X-ray weakness of WLQs is mainly due to the absorption rather than a result of them being intrinsically X-ray weak. Then a shielding-gas scenario was proposed to unify these two WLQ subtypes. In this picture WLQs are all intrinsically similar, with X-ray weak WLQs being observed at larger inclination angles through a geometrically thick inner disc region (or a puffed-up/slim inner disc region), which blocks the line-of-sight to the nuclear X-ray emission (e.g. Wu et al. 2011; Luo et al. 2015). The puffed-up region may also act as a screen which shields the BLR and NLR from the nuclear ionising continuum, resulting in much weaker UV/optical emission lines. The high mass accretion rate of WLQs ( $L_{\text{bol}}/L_{\text{Edd}} \gtrsim 1$ ) also supports the existence of such a puffed-up inner disc region (e.g. Abramowicz et al. 1988; Ohsuga & Mineshige 2011; Netzer & Trakhtenbrot 2014).

We notice that the unified picture of super-Eddington NLS1s presented in this work is similar to that suggested for WLQs. The differences between ‘simple’ and ‘complex’ NLS1s are quite similar to the differences between the two WLQ subtypes. The two NLS1 subtypes have similar intrinsic optical/UV spectra (except the host galaxy emission), but the X-ray emission of ‘complex’ NLS1s can be much fainter (Fig. 10). These NLS1s and WLQs are all accreting near/above the Eddington limit, and they all show intrinsically weak forbidden lines such as [O III]  $\lambda$ 5007. Therefore, from one aspect the unified scenario of WLQs based on the inclination angle also support a similar unified scenario for super-Eddington NLS1s.

However, UV emission lines in NLS1s and bright quasar composite spectra are much stronger than those in WLQs, in particular the C IV and Si IV lines. This implies that the shielding material in NLS1s must be located at a larger radius than that of the C IV and Si IV emitting region. Since NLS1s typically have black hole masses of 1-3 orders of magnitude smaller than quasars, their  $\dot{m}_{\text{out}}$  can be much more super-Eddington and their disc can be much hotter, so the radius where the disc becomes geometrically thick can be much larger as well. Luo et al. (2015) showed that the puffed-up disc radius in WLQs is a few tens of  $R_g$ , while we showed that for RX J0439.6-5311 the  $R_{\text{crit}}$  can be hundreds of  $R_g$  (Section 6.3). Therefore, the difference in the UV emission lines between NLS1s and WLQs can be explained by differ-

ent relative locations and sizes of their puffed-up inner disc regions.

In effect we could consider these super-Eddington NLS1s as the low redshift analogs of WLQs, with ‘simple’ NLS1s corresponding to X-ray normal WLQs, and ‘complex’ NLS1s corresponding to X-ray weak WLQs. However, there are still some questions that remain to be answered. For example, NLS1s are likely to have higher Eddington ratios than WLQs, and a disc wind may play a more critical role. Indeed, Gardner & Done (2015) and Hagino et al. (2016) have shown that the obscuration by clumps in the disc wind can reproduce the observed X-ray light curves and spectra of 1H 0707-495. It is not clear whether or not the presence of a disc wind plays a significant role in the X-ray weakness of some WLQs. Additional X-ray variability is expected if there is strong wind absorption in an X-ray weak WLQ, but the timescale of this variability may scale up as the black hole mass, thereby making the variability difficult to detect in a single observation. We cannot find any study on the long-term X-ray variability in any X-ray weak WLQs. Another question is that whether the disc wind in NLS1s could also be responsible for their weak Oxygen forbidden lines or not. Moreover, if the Eddington ratio is the only key parameter required to explain the weak optical/UV lines in WLQs, then we should expect the same phenomena in all super-Eddington quasars. But this is clearly not the case in PG 1247+267, which is a non-WLQ at  $z = 2.038$  with well measured  $L_{\text{bol}}/L_{\text{Edd}} = 11$  (Trevese et al. 2014; Bentz & Katz 2015; Lanzuisi et al. 2016). So there must be some other important parameters affecting the optical/UV line intensity. Future studies of these super-Eddington AGN are necessary in order to obtain a deeper understanding of these most extreme accretion flows in the universe.

## 7 SUMMARY AND CONCLUSIONS

In this paper we report the results from one of the most detailed multi-wavelength studies of an unobscured, highly super-Eddington QSO RX J0439.6-5311. Firstly we found a better redshift of 0.242 for this source. Then the excellent multi-wavelength data-set enables us to make confident estimates of its  $L_{\text{bol}}$  ( $\sim 20\%$  uncertainty). Our results clearly indicate that it is one of the most robust ‘super-Eddington’ source. For a black hole mass of  $(5-10) \times 10^6 M_{\odot}$ , we measure  $L_{\text{bol}}/L_{\text{Edd}} = 2.7 - 6.5$  and  $\dot{m}_{\text{out}} = 5.9 - 23.8$ .

With the above  $M$ ,  $L_{\text{bol}}$  and  $\dot{m}_{\text{out}}$ , the multi-wavelength properties of the super-Eddington accretion flow in RX J0439.6-5311 can be summarised in the unified picture in Fig. 11. The key aspects of this picture include the following:

- the outer part of the accretion flow is consistent with the standard thin disc model outside of  $190-380 R_g$  for a black hole mass of  $5 - 10 \times 10^6 M_{\odot}$ . This is suggested by the underlying continua in the optical/UV spectra observed down to  $900 \text{ \AA}$ .
- within a critical radius (e.g.  $140 - 170 R_g$  for  $M = 1 \times 10^7 M_{\odot}$  and  $\dot{m}_{\text{out}} = 5.9$ ), the accretion disc starts to deviate from a standard thin disc model because of a strong disc wind and/or advection, as could be expected in such high mass accretion rate flows, which carries away a significant

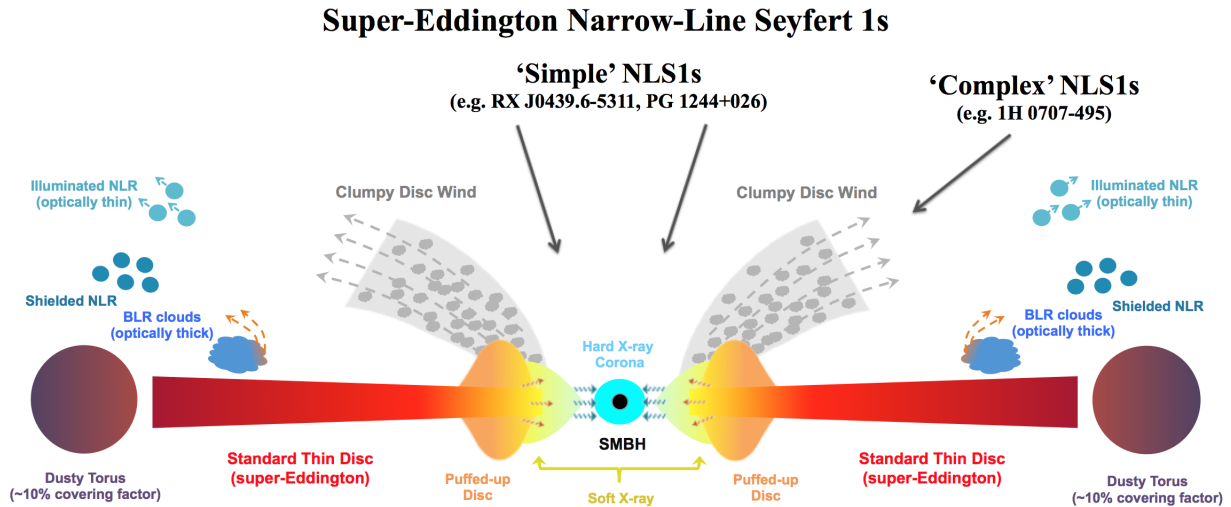


**Figure 11.** A schematic cartoon of the super-Eddington accretion flow in RX J0439.6-5311 based on the results of our multi-wavelength study. We propose that this accretion flow picture may also be applicable for super-Eddington NLS1s such as PG 1244+026, 1 H0707-495, Mrk 335, etc, with the apparent differences in their X-ray emission caused by the viewing angle effect relative to the clumpy disc wind (see Section 6.3 for detailed descriptions related to this picture).

amount of the gravitational energy in the disc. This is supported by the large difference between  $L_{\text{bol}}/L_{\text{Edd}}$  and  $\dot{m}_{\text{out}}$  in Table 3, as well as the SED discrepancy in the far-UV and soft X-ray band shown in Fig. 7.

- at some radii of at least tens of  $R_g$  away from the black hole, there exists a low temperature thermal electron population, which up-scatters disc photons into the soft X-ray band to produce the prominent soft excess. Then some of these soft X-ray photons meet the hot corona at small radii and are up-scattered into the hard X-ray band. This inner disc structure is supported by the results of X-ray spectral-timing study in Paper-I. We also find tentative evidence for the connection between the soft X-ray region and the puffed-up inner disc region.

- The geometrically thick inner disc and/or the clumpy disc wind can shield part of NLR from the nuclear ionising continuum, thereby reducing the strength of forbidden lines in the NLR such as [O III]. The extremely powerful radiation may also trigger a global outflow in the [O III] emitting NLR. The disc radiation may also be strong enough to trigger an outflow on the surface of the optically thick BLR clouds. Evidence for this is found in the line profiles of [O III] $\lambda$ 5007 and H $\beta$  (see Fig. 2).

- the hot dust in the torus has a covering factor of 10.8% and produces essentially all of the near-IR emission (see Fig. 7).

RX J0439.6-5311 also allows us to constrain the  $x$  factor in the  $L_{\text{bol}}/L_{\text{Edd}} = 1 + x \ln \dot{m}_{\text{out}}$  relation to be  $0.95 \leq x \leq 1.72$ . Using a simulation based on the standard accretion disc model, we can rule out the possibility of detecting any reprocessed X-ray variability in the optical/UV disc emission, but a significant long-term optical/UV/X-ray covariance has been observed, which is likely caused by the long-term fluctuation of  $\dot{m}_{\text{out}}$ .

Furthermore, we compare RX J0439.6-5311 with two

other super-Eddington NLS1s PG 1244+026 and 1H 0707-495. We found that RX J0439.6-5311 behaves as a ‘simple’ NLS1 in terms of its X-ray emission and broadband SED, but it is more similar to a ‘complex’ NLS1 such as 1H 0707-495 in the optical/UV spectra. Therefore, the scenario we proposed for the super-Eddington accretion flow in RX J0439.6-5311 is likely to be applicable for both ‘simple’ and ‘complex’ super-Eddington NLS1 subtypes. Then different inclination angles lead to different line-of-sights to the nuclear X-ray emitting region, which then result in the observed differences in their X-ray spectra due to the possible passage of the line-of-sight through the clumpy wind material (see Fig. 11). Currently, a sample of representative NLS1s of high mass accretion rates is under our investigation in order to further verify this unified scenario. The results will be reported in the near future.

Finally, we also compare super-Eddington NLS1s with WLQs, finding that these two AGN populations share a range of similar properties from optical to hard X-rays, and that the inclination angle plays a crucial role in both of them. Therefore, we propose that the super-Eddington NLS1s could be the low-redshift analogs of WLQs at high redshift. However, there are also some obvious spectral variability differences between these extreme NLS1s and WLQs, which are probably caused by the large difference in their black hole masses and spins. Future work is required to compare these two AGN populations in more detail.

## ACKNOWLEDGEMENTS

We thank Dirk Grupe for kindly providing the unique optical spectrum of RX J0439.6-5311 observed with the ESO’s 1.52 m telescope. The anonymous referee is appreciated for providing valuable comments and suggestions to improve the paper. CJ acknowledges the support by the Bun-



desministerium für Wirtschaft und Technologie/Deutsches Zentrum für Luft- und Raumfahrt (BMWI/DLR, FKZ 50 OR 1408 and FKZ 50 OR 1604) and the Max Planck Society. CD and MJW acknowledge STFC funding under grant ST/L00075X/1.

This work is mainly based on a recent observation conducted by *XMM-Newton*, an ESA science mission with instruments and contributions directly funded by ESA Member States and the USA (NASA). We have made use of the *ROSAT* Data Archive of the Max-Planck-Institut für extraterrestrische Physik (MPE) at Garching, Germany. We acknowledge the use of public data from the *Swift* data archive. This work also makes use of observations conducted by the NASA/ESA Hubble Space Telescope, with public data obtained from the Mikulski Archive for Space Telescopes (MAST). STScI is operated by the Association of Universities for Research in Astronomy, Inc., under NASA contract NAS5-26555. Support for MAST for non-*HST* data is provided by the NASA Office of Space Science via grant NNX09AF08G and by other grants and contracts. This work involves data products from the Wide-field Infrared Survey Explorer, which is a joint project of the University of California, Los Angeles, and the Jet Propulsion Laboratory/California Institute of Technology, funded by the National Aeronautics and Space Administration. We use data products from the Two Micron All Sky Survey, which is a joint project of the University of Massachusetts and the Infrared Processing and Analysis Center/California Institute of Technology, funded by the National Aeronautics and Space Administration and the National Science Foundation. This research has made use of the NASA/IPAC Extragalactic Database (NED) which is operated by the Jet Propulsion Laboratory, California Institute of Technology, under contract with the National Aeronautics and Space Administration.

## REFERENCES

- Abramowicz M. A., Czerny B., Lasota J. P., Szuszkiewicz E., 1988, *ApJ*, 332, 646
- Ai Y. L., Yuan W., Zhou H., Wang T. G., Dong X. B., Wang J. G., Lu H. L., 2013, *AJ*, 145, 90
- Antonucci R., 1993, *ARA&A*, 31, 473
- Arévalo P., Papadakis I., Kuhlbrodt B., Brinkmann W., 2005, *A&A*, 430, 435
- Alston W. N., Done C., Vaughan S., 2014, *MNRAS*, 439, 1548
- Alston W. N., Vaughan S., Uttley P., 2013, *MNRAS*, 429, 75
- Arnaud K. A., 1996, *ASPC*, 101, 17
- Barger A. J., Cowie L. L., 2010, *ApJ*, 718, 1235
- Baskin A., Laor A., Stern J., 2014b, *MNRAS*, 438, 604
- Baskin A., Laor A., Stern J., 2014a, *MNRAS*, 445, 3025
- Bentz M. C., Katz S., 2015, *PASP*, 127, 67
- Bessell M. S., 1991, *A&A*, 242, L17
- Bisnovatyi-Kogan G. S., Blinnikov S. I., 1977, *A&A*, 59, 111
- Blandford R. D., McKee C. F., 1982, *ApJ*, 255, 419
- Boller T., Brandt W. N., Fink H., *A&A*, 305, 53
- Boroson T. A., 2002, *ApJ*, 565, 78
- Boroson T. A., Green R. F., 1992, *ApJS*, 80, 109
- Brandt W. N., Mathur S., Elvis M., 1997, *MNRAS*, 285, L25
- Buisson D. J. K., Lohfink A. M., Alston W. N., Fabian A. C., 2017, *MNRAS*, 464, 3194
- Chiang C. Y., Walton D. J., Fabian A. C., Wilkins D. R., Gallo L. C., 2015, *MNRAS*, 446, 759
- Crummey J., Fabian A. C., Gallo L., Ross R. R., 2006, *ApJ*, 365, 1067
- Davis S. W., Hubeny I., 2006, *ApJS*, 164, 530
- Davis S. W., Laor A., 2011, *ApJ*, 728, 98
- Danforth C. W., et al., 2016, *ApJ*, 817, 111
- Diamond-Stanic A. M., et al., 2009, *ApJ*, 699, 782
- Done C., Davis S. W., 2008, *ApJ*, 683, 389
- Done C., Jin C., 2016, *MNRAS*, 460, 1716
- Done C., Nayakshin S., 2007, *MNRAS*, 377, L59
- Done C., Jin C., Middleton M., Ward M., 2013, *MNRAS*, 434, 1955
- Done C., Davis S. W., Jin C., Blaes O., Ward M., 2012, *MNRAS*, 420, 1848
- Dopita M. A., et al., 2015, *ApJS*, 217, 12
- Edelson R., et al., 2015, *ApJ*, 806, 129
- Eggum G. E., Coroniti F. V., Katz J. I., 1988, *ApJ*, 330, 142
- Fabian A. C., Miniutti, G., 2005, *arXiv:astro-ph/0507409*
- Fabian A. C., et al., 2009, *Nature*, 459, 540
- Fabian A. C., et al., 2013, *MNRAS*, 429, 2917
- Fanidakis N., Baugh C. M., Benson A. J., Bower R. G., Cole S., Done C., Frenk C. S., 2011, *MNRAS*, 410, 53
- Francis P. J., Hewett P. C., Foltz C. B., Chaffee F. H., Weymann R. J., Morris S. L., 1991, *ApJ*, 373, 465
- Gardner E., Done C., 2014, *MNRAS*, 442, 2456
- Gardner E., Done C., 2015, *MNRAS*, 448, 2245
- Gardner E., Done C., 2017, *MNRAS*, in print (*arXiv:1603.09564*)
- Gallo L. C., 2006, *MNRAS*, 368, 479
- Gierliński M., Done C., 2004, *MNRAS*, 349, L7
- Gierliński M., Middleton M., Ward M., Done C., 2008, *Nature*, 455, 369
- Grupe D., 2004b, *AJ*, 127, 1799
- Grupe D., Wills B. J., Leighly K. M., Meusinger H., 2004a, *AJ*, 127, 156
- Grupe D., Komossa S., Leighly K. M., Page K. L., 2010, *ApJS*, 187, 64
- Hagino K., Odaka H., Done C., Tomaru R., Watanabe S., Takahashi T., 2016, *MNRAS*, 461, 3954
- Hashizume K., Ohsuga K., Kawashima T., Tanaka M., 2015, *PASJ*, 67, 58
- Husemann B., Jahnke K., Sánchez S. F., Wisotzki L., Nugroho D., Kupko D., Schramm M., 2014, *MNRAS*, 443, 755
- Jansen F., Lumb D., Altieri B., et al., 2001, *A&A*, 365, L1
- Jiang Y. F., Davis S. W., Stone J. M., 2016, *ApJ*, 827, 10
- Jiang Y. F., Stone J. M., Davis S. W., 2013, *ApJ*, 778, 65
- Jiang Y. F., Stone J. M., Davis S. W., 2014, *ApJ*, 796, 106
- Jin C., Done C., Ward M., 2016, *MNRAS*, 455, 691
- Jin C., Done C., Ward M., 2017, *MNRAS*, 468, 3663
- Jin C., Done C., Middleton M., Ward M., 2013, *MNRAS*, 436, 3173
- Jin C., Ward M., Done C., 2012b, *MNRAS*, 422, 3268
- Jin C., Ward M., Done C., 2012c, *MNRAS*, 425, 907
- Jin C., Ward M., Done C., Gelbord J., 2012a, *MNRAS*, 420, 1825
- Kalberla P. M. W., Burton W. B., Hartmann D., Arnal E. M., Bajaja E., Morras R., Pöppel W. G. L., 2005, *A&A*, 440, 775
- Kara E., Alston W. N., Fabian A. C., Cackett E. M., Uttley P., Reynolds C. S., Zoghbi A., 2016, *MNRAS*, 462, 511
- Kara E., Fabian A. C., Cackett E. M., Steiner J. F., Uttley P., Wilkins D. R., Zoghbi A., 2013c, *MNRAS*, 428, 2795
- Kaspi S., Smith P. S., Netzer H., Maoz D., Jannuzi B. T., Giveon U., 2000, *ApJ*, 533, 631
- Keeney B. A., Stocke J. T., Rosenberg J. L., Danforth C. W., Ryan-Weber E. V., Shull J. W., Savage B. D., Green J. C., 2013, *ApJ*, 765, 27
- King A. R., Pringle J. E., Hofmann J. A., 2008, *MNRAS*, 385, 1621
- Kovačević J., Popović L. Č., Dimitrijević M. S., 2010, *ApJS*, 189, 15
- Lanzuisi G., et al., 2016, *A&A*, 590, A77



- Laor A., Davis S. W., 2014, *MNRAS*, 438, 3024
- Laor A., Fiore F., Elvis M., Wilkes B. J., McDowell J. C., 1997, *ApJ*, 477, 93
- Leighly K. M., 2004, *ApJ*, 611, 125
- Leighly K. M., Moore J. R., 2004, *ApJ*, 611, 107
- Leighly K. M., Halpern J. P., Jenkins E. B., Casebeer D., 2007, *ApJS*, 173, 1
- Lipunova G. V., 1999, *Astronomy Letters*, 25, 508
- Lohfink A. M., Reynolds C. S., Vasudevan R., Mushotzky R. F., Miller N. A., 2014, *ApJ*, 788, 10
- Luo B., et al., 2015, *ApJ*, 805, 122
- Magdziarz P., Blaes O. M., Zdziarski A. A., Johnson W. N., Smith D. A., 1998, *MNRAS*, 301, 179
- Marconi A., Axon D. J., Maiolino R., Nagao T., Pastorini G., Pietrini P., Robinson A., Torricelli G., 2008, *ApJ*, 678, 693
- Markwardt C. B., 2009, *Astronomical Data Analysis Software and Systems XVIII*, 411, 251
- Mason K. O., et al., 2002, *ApJL*, 580, L117
- M<sup>c</sup>Hardy I. M., Arévalo P., Uttley P., Papadakis I. E., Summons D. P., Brinkmann W., Page M. J., 2007, *MNRAS*, 382, 985
- Meusinger H., Weiss V., 2013, *A&A*, 560, A104
- McLure R. J., Jarvis M. J., 2002, *MNRAS*, 337, 109
- Middleton M., Done C., Ward M., Gierliński M., Schurch N., 2009, *MNRAS*, 394, 250
- Miller L., Turner T. J., Reeves J. N., George I. M., Kraemer S. B., Wingert B., 2007, *A&A*, 463, 131
- Miniutti G., Fabian A. C., 2004, *MNRAS*, 349, 1435
- Miniutti G., Ponti G., Greene J. E., Ho L. C., Fabian A. C., Iwasawa K., 2009, *MNRAS*, 394, 443
- Netzer H., Trakhtenbrot B., 2014, *MNRAS*, 438, 672
- Okuda T., Teresi V., Toscano E., Molteni D., 2005, *MNRAS*, 357, 295
- Ohsuga K., Mineshige S., 2011, *ApJ*, 736, 2
- Ohsuga K., Mori M., Nakamoto T., Mineshige S., 2005, *ApJ*, 628, 368
- Orban de Xivry G., Davies R., Schartmann M., Komossa S., Marconi A., Hicks E., Engel H., Tacconi, L., 2011, *MNRAS*, 417, 2721
- Osterbrock D. E., Pogge R. W., 1985, *ApJ*, 297, 166
- Pei Y. C., 1992, *ApJ*, 395, 130
- Peterson B. M., 2014, *SSRv*, 183, 253
- Peterson B. M., et al., 2014, *ApJ*, 795, 149
- Plotkin R. M., et al., 2010a, *AJ*, 139, 390
- Plotkin R. M., et al., 2010b, *ApJ*, 721, 562
- Polletta M., et al., 2007, *ApJ*, 663, 81
- Ponti G., Papadakis I., Bianchi S., Guainazzi M., Matt G., Uttley P., Bonilla N. F., 2012, *A&A*, 542, A83
- Ponti G., et al., 2010, *MNRAS*, 406, 2591
- Poutanen J., Lipunova G., Fabrika S., Butkevich A. G., Abolmasov P., 2007, *MNRAS*, 377, 1187
- Richards G. T., et al., 2006, *ApJS*, 166, 470
- Robertson D. R. S., Gallo L. C., Zoghbi A., Fabian A. C., 2015, *MNRAS*, 453, 3455
- Ross R. R., Fabian A. C., 2005, *MNRAS*, 358, 211
- Sądowski A., Narayan R., McKinney J. C., Tchekhovskoy A., 2014, *MNRAS*, 439, 503
- Sądowski A., Narayan R., Tchekhovskoy A., Abarca D., Zhu Y., McKinney J. C., 2015, *MNRAS*, 447, 49
- Shen Y., Ho L. C., 2014, *Nature*, 513, 210
- Silva L., Maiolino R., Granato G. L., 2004, *MNRAS*, 355, 973
- Shakura N. I., Sunyaev R. A., 1973, *A&A*, 24, 337
- Shang Z., et al., 2005, *ApJ*, 619, 41
- Shapovalova A. I., et al., 2012, *ApJS*, 202, 10
- Shemmer O., Lieber S., 2015, *ApJ*, 805, 124
- Shemmer O., Brandt W. N., Netzer H., Maiolino R., Kaspi S., 2006, *ApJL*, 646, L29
- Shemmer O., et al., 2009, *ApJ*, 696, 580
- Shull J. M., Stevans M., Danforth C. W., 2012, *ApJ*, 752, 162
- Sim S. A., Proga D., Miller L., Long K. S., Turner T. J., 2010, *MNRAS*, 408, 1396
- Smith R., Vaughan S., 2007, *MNRAS*, 375, 1479
- Takeuchi S., Ohsuga K., Mineshige S., 2014, *PASJ*, 66, 48
- Tatum M. M., Turner T. J., Sim S. A., Miller L., Reeves J. N., Patrick A. R., Long K. S., 2012, *ApJ*, 752, 94
- Telfer R., Zheng W., Kriss G. A., Davidsen A. F., 2002, *ApJ*, 656, 773
- Timmer J., Koenig M., 1995, *A&A*, 300, 707
- Thomas H. C., Beuermann K., Reinsch K., Schwobe A. D., Truemper J., Voges W., 1998, *A&A*, 335, 467
- Trevese D., Perna M., Vagnetti F., Saturni F. G., Dadina M., 2014, *ApJ*, 795, 164
- Turner T. J., Miller L., Reeves J. N., Kraemer S. B., 2007, *A&A*, 475, 121
- Unger S. W., et al., 1987, *MNRAS*, 228, 671
- Vanden Berk D. E., et al., 2001, *AJ*, 122, 549
- Vasudevan R. V., Fabian A. C., 2007, *MNRAS*, 381, 1235
- Vasudevan R. V., Fabian A. C., 2009, *MNRAS*, 392, 1124
- Vaughan S., Edelson R., Warwick R. S., Uttley P., 2003, *MNRAS*, 345, 1271
- Verner D. A., Ferland G. J., Korista K. T., Yakovlev D. G., 1996, *ApJ*, 465, 487
- Vestergaard M., 2002, *ApJ*, 571, 733
- Vestergaard M., Peterson B. M., 2006, *ApJ*, 641, 689
- Wang J. M., Netzer H., 2003, *A&A*, 398, 927
- Watarai K., Fukue J., Takeuchi M., Mineshige S., 2000, *PASJ*, 52, 133
- Wilms J., Allen A., McCray R., 2000, *ApJ*, 542, 914
- Woo J. H., Urry C. M., 2002, *ApJ*, 579, 530
- Wright E. L., 2006, *PASP*, 118, 1711
- Wu J., et al., 2011, *ApJ*, 736, 28
- Wu J., et al., 2012, *ApJ*, 747, 10
- Zheng W., Kriss G. A., Telfer R. C., Grimes J. P., Davidsen A. F., 1997, *ApJ*, 475, 469
- Zoghbi A., Fabian A. C., Uttley P., Miniutti G., Gallo L. C., Reynolds C. S., Miller J. M., Ponti G., 2010, *MNRAS*, 401, 2419
- Zu Y., Kochanek C. S., Peterson B. M., 2011, *ApJ*, 735, 80

This paper has been typeset from a  $\text{\TeX}/\text{\LaTeX}$  file prepared by the author.